

Cross Flow Instability of the Supersonic Flow over a 4:1 Elliptic Cone

S. L. Huang
G. K. Stuckert
Th. Herbert

DynaFlow, Inc.
Columbus, Ohio, 43221-0319, USA

January 1995

Final Report
Contract F49620-94-C-0053
Air Force Office of Scientific Research
Bolling AFB, DC 20332-0001

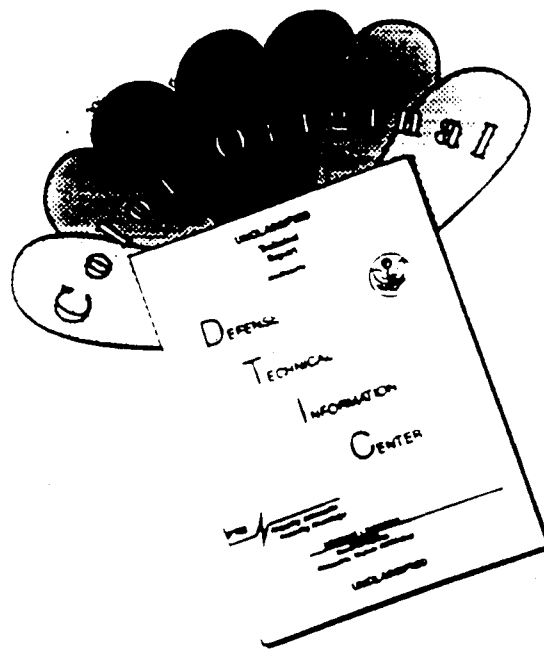
Accession For	
NTIS	CRA&I <input checked="" type="checkbox"/>
DTIC	TAB <input type="checkbox"/>
Unannounced <input type="checkbox"/>	
Justification _____	
By _____	
Distribution / _____	
Availability Codes	
Dist	Avail and/or Special
A-1	

DTIC QUALITY INSPECTED 4

19950214 016

REPORT DOCUMENTATION PAGE			Form Approved OMB No. 0704-0188	
Public reporting burden for this collection of information is estimated to average 1 hour per response, including the time for reviewing instructions, searching existing data sources, gathering and maintaining the data needed, and completing and reviewing the collection of information. Send comments regarding this burden estimate or any other aspect of this collection of information, including suggestions for reducing this burden, to Washington Headquarters Services, Directorate for Information Operations and Reports, 1215 Jefferson Davis Highway, Suite 1204, Arlington, VA 22202-4302, and to the Office of Management and Budget, Paperwork Reduction Project (0704-0188), Washington, DC 20503.				
1. AGENCY USE ONLY (Leave blank)	2. REPORT DATE Jan. 20, 1995	3. REPORT TYPE AND DATES COVERED Final 6/1/94 - 1/31/95		
4. TITLE AND SUBTITLE Crossflow Stability of Supersonic Flow over an Elliptic Cone		5. FUNDING NUMBERS F49620-94-C-0053 2307/AS		
6. AUTHOR(S) S. L. Huang, G. K. Stuckert, Th. Herbert				
7. PERFORMING ORGANIZATION NAME(S) AND ADDRESS(ES) DynaFlow, Inc. 3040 Riverside Dr. Columbus, OH 43221		8. PERFORMING ORGANIZATION REPORT NUMBER AFOSR-TR- 95 0077		
9. SPONSORING/MONITORING AGENCY NAME(S) AND ADDRESS(ES) USAF, AFMC AFOSR/NA Air Force Office of Scientific Research 110 Duncan Avenue Suite B115 Bolling AFB DC 20332-0001		10. SPONSORING/MONITORING AGENCY REPORT NUMBER F49620-94-C-0053		
11. SUPPLEMENTARY NOTES DTIC ELECTE FEB 23 1995 S G D				
12a. DISTRIBUTION/AVAILABILITY STATEMENT Approved for public release, distribution unlimited		12b. DISTRIBUTION CODE		
13. ABSTRACT (Maximum 200 words) The crossflow-initiated transition process over the surface of a supersonic 4:1 elliptic cone with 17.5 degree half-angle has been investigated using state-of-the-art local and PSE stability analyses. The basic flow was computed using the AFWAL PNS code. The local stability analysis was performed in order to find the regions and parameter ranges in which the crossflow vortex is unstable. The PSE analyses were then carried out in order to study the nonparallel effects of the flow on the most dangerous vortices--those with the greatest growth. The PSE analyses predict much greater amplification of the crossflow vortices and transition near the apex of the cone compared to the local analysis.				
14. SUBJECT TERMS elliptic cone supersonic flow crossflow stability		PSE analysis		15. NUMBER OF PAGES 48
17. SECURITY CLASSIFICATION OF REPORT		18. SECURITY CLASSIFICATION OF THIS PAGE		16. PRICE CODE
19. SECURITY CLASSIFICATION OF ABSTRACT		20. LIMITATION OF ABSTRACT		

DISCLAIMER NOTICE



THIS DOCUMENT IS BEST QUALITY AVAILABLE. THE COPY FURNISHED TO DTIC CONTAINED A SIGNIFICANT NUMBER OF COLOR PAGES WHICH DO NOT REPRODUCE LEGIBLY ON BLACK AND WHITE MICROFICHE.

Contents

1	Introduction	2
2	Accomplishments	3
3	Basic Flow	3
4	Stability Analysis	4
5	Grid of Basic Flow Computation	5
6	Results of the Basic Flow Computation	6
7	Results of the Local Stability Analysis	7
8	Results of the PSE Analysis	8
9	Conclusion	9
10	Appendix A: Reference Data and Conversions	10
11	References	11
12	Figures	13

1 Introduction

The interest in theoretical and experimental analysis of the stability of supersonic flows has been focused on the traveling waves that are precursor of transition in two-dimensional boundary layers. These analyses have been guided by extensive results of Mack (1984) on the changing characteristics of dominant instabilities as the Mach number increases. In contrast to low speeds, where Squire's theorem predicts dominance of two-dimensional waves, oblique waves exhibit stronger growth in flat-plate boundary layers at supersonic Mach numbers. Besides the first mode, additional higher modes appear. At $Ma \approx 4$, the two-dimensional second mode exhibits the strongest growth.

Various experiments in high-speed flows have been conducted to verify the theoretical predictions (Kendall 1975, Demetriades 1977) and to study these phenomena in more general boundary layers. Most of the latter experiments concern sharp or blunt axisymmetric cones at zero angle of attack (Stetson et al. 1983, Stetson et al. 1984). The growth characteristics of wave-type first and second modes have been documented in some detail. The significant difference between the experimental data for sharp and blunt cones has stimulated intense theoretical/computational efforts (Mack 1986, Malik et al. 1990, Herbert et al. 1992, Simen 1992). Much of these efforts has been consumed by the need to obtain accurate basic flows especially for blunt cones. Traditional numerical methods are tuned to provide reasonable surface pressure and temperature distributions but reveal flaws in the flow field (Ramakrishnan et al. 1993) that affect the stability characteristics. Improved numerical methods for basic flow computations are yet to be developed. The available information, however, gives guidance on how to utilize the existing codes for best results and what quantitative changes to expect from certain approximations, e.g. the use of PNS. The efforts to improve the stability analysis for a given basic flow and to abandon unnecessary simplifications such as the neglect of curvature effects have been successful and the results of different investigators have converged in a narrow band.

The stability of three-dimensional supersonic boundary layers has been addressed only in a few studies. On cones at angle of attack or bodies of non-circular cross-section, crossflow instability is likely to occur. Cross-flow vortices have been observed on swept cylinders at $Ma = 10$ (Arnal 1991) and made visible with thermo-sensitive paints at $Ma = 8$ on circular cones at angle of attack (Oberkampf et al. 1992, Aeschliman 1992). Detailed stability measurements on a sharp cone at angle of attack (Stetson et al. 1985) have been restricted to the windward and leeward planes of symmetry. The growth characteristics of crossflow instabilities and the crossflow-initiated transition process in supersonic flows are currently unknown.

While the past interest in high-speed instabilities was largely spurred by axisymmetric rockets and missiles, the design of advanced aerodynamic vehicles for high-speed flight requires insight and analytical capabilities for a wider class of instabilities in more general three-dimensional flows. Both experimental and theoretical

efforts should be conducted to establish the fundamental aspects of instabilities in three-dimensional supersonic boundary layers.

2 Accomplishments

Under this contract F49620-94-C-0053 with the Air Force Office of Scientific Research, a study on the characteristics of the crossflow vortex on the surface of a 4:1 elliptic cone with a 17.5° half-angle on the major axis was conducted. In particular, the following tasks were completed:

- A. Computation of the basic flow over an elliptic cone using the AFWAL PNS code with a sufficient number of grid points in all three spatial directions to obtain results suitable for stability analysis.
- B. Documentation of the basic-flow field, especially the surface quantities (pressure, shear stress, and temperature) and the relative strength of the crossflow component.
- C. Parametric study of instabilities with respect to steady and unsteady crossflow vortices and waves of selected frequencies. This study has been performed using the local approach as implemented in our linear stability code LISA.
- D. PSE analysis of linear crossflow vortices for the "most dangerous" parameter combinations selected from item C. This analysis has provided amplitude growth curves and N factors.
- E. Characterization of variations in surface quantities associated with crossflow vortices. Knowledge of the amplitude of periodic variations in pressure, shear stress, and temperature enables the selection of proper sensors for data acquisition.

More detail on the various tasks is given in the following sections.

During this work the authors were in frequent technical contact with Steve Schneider of Purdue University through e-mail, fax, and phone to support the construction of a proper model for his planned experiments. The data used for our analysis match the experimental conditions and requirements. On November 18, 1994, Th. Herbert and S. Huang visited Purdue University for a presentation on the PSE method and discussions of our results for the elliptic cone with S. Schneider and his colleagues.

3 Basic Flow

The basic flow on the cone was computed using the AFWAL parabolized Navier-Stokes (PNS) code (Stalnaker et al. 1986). The PNS code computes the solution

of the parabolized steady state Navier-Stokes equations which neglect diffusion in the streamwise direction. In the subsonic boundary layer, the streamwise pressure gradient is approximated by a "sublayer model". Because the PNS flow code is based on the steady state parabolized Navier-Stokes equations, the computational expense is significantly smaller than a true Navier-Stokes solver owing to the fact that only space marching is necessary in the streamwise direction.

To start the computation, a conical step-back procedure was used to provide an approximate conical solution on a plane near the apex. This procedure makes use of a conical coordinate system and assumes that the flow is locally conical. An iterative integration between the first and second planes needs to be carried out until the solution is the same on the same conical rays. The conical step-back procedure has already been implemented in the AFWAL PNS code. The solution obtained from the conical step-back procedure was then used as an initial condition for the integration of the PNS equations in the streamwise direction. Different grids have been used to estimate the effect on stability characteristics.

4 Stability Analysis

The stability analysis was carried out using the traditional linear stability analysis and the advanced PSE codes developed at DynaFlow, Inc. (Herbert et al. 1993).

The local stability analysis is based on the assumption that the flow is locally parallel and the disturbances are small. It provides the local stability characteristics of the flow. In the local stability analysis, the disturbance \tilde{Q} to the basic state is assumed to follow the normal mode assumption, e.g.,

$$\tilde{Q} = \mathbf{f} \cdot e^{i(\alpha x + \beta \theta - \omega t)}$$

where α and β are the streamwise and circumferential wave numbers, respectively, ω is the frequency, and \mathbf{f} is the eigenfunction. In general, the above quantities are all complex. In this research, however, β is kept real. In the spatial stability analysis, ω is assumed to be real, and $-\alpha_i$ is the growth rate of the normal mode. Substitution of the normal mode assumption into the disturbance equations leads to an eigenvalue problem which is solved by either the spectral or finite difference method. In this research, the local stability analysis was used to search for the unstable flow regions and parameter combinations.

The flow over the elliptic cone is three dimensional. The nonparallel effects owing to the streamwise growth of shock layer and boundary layer as well as the azimuthal variation are neglected in the local stability analysis. The PSE method was used to analyze the nonparallel effects on the stability characteristics of the crossflow vortex. The azimuthal variations still have to be neglected owing to the unavailability of a stability theory for three-dimensional flows.

The PSE code solves the parabolized stability equations which are derived from the Navier-Stokes disturbance equations by neglecting the small second order derivatives

of the shape functions in the streamwise coordinate direction (Herbert 1993). This generates an initial-boundary-value problem which can be solved by a space marching method. The initial conditions for the PSE analysis are provided by the solutions from the local stability analysis. Like the local stability analysis code, the PSE code generates the shape functions and the complex spatial wave number α as a function of the marching variable. Since the PSE code considers all important terms in the stability equations, it is a powerful engineering tool in analyzing the linear or nonlinear evolution of disturbances in the parallel or nonparallel flow field. Moreover, because of its parabolized nature, the PSE approach is much faster in comparison with the Navier-Stokes PNS codes. The PSE analysis code has been extensively used to study the stabilities of flows over a sharp cone and a blunt cone at an angle of attack at $M_a = 8$ (Herbert et al. 1993).

In the stability analysis, all the quantities are scaled by appropriate values. In particular, all the lengths are scaled by $\sqrt{\nu_\infty L/V_\infty}$ ($= 1.87034 \cdot 10^{-4}m = 7.3635 \cdot 10^{-3}in$) 6 inches away from the apex; the density, temperature and velocities are scaled by their free stream values; the Prandtl number is assumed to be 0.72.

5 Grid of Basic Flow Computation

A curvilinear coordinate system ξ^1, ξ^2, ξ^3 (shown in Figure 1) is used for the computation of the basic flow over the elliptic cone. These coordinates are for the axial, radial and azimuthal coordinates, respectively.

Figure 2 shows a cross section of half of the 4:1 elliptic cone. In the following, the location on the cone surface at a particular streamwise distance from the apex is specified by the angle θ measured from the minor axis.

The computational grid is arranged such that the radial grid lines are spaced in equal angle increments in the circumferential direction. In the circumferential direction, 111 grid points in half of the cone periphery were used for the basic flow computation. In the streamwise direction, the step size corresponds to a Courant number of 30 (the PNS code automatically checks and corrects the step size to make the algorithm stable). The input file to the PNS was setup in such a way that the data was output every 4 planes to save disk space. Figure 3 shows the computational grid generated from the PNS output on 1/4 of the unfolded cone surface. The horizontal line at the bottom corresponds to the minor axis and the skewed line at the top corresponds to the major axis. The slightly curved vertical lines represent the circumferential lines of equal ξ^1 on the cone's surface.

In the radial direction, both 251 radial points and 501 radial points were used. Then a local stability analysis was conducted to investigate the sensitivity of the stability results to the basic flow. In Figure 4, α_i is plotted against ξ^1 using the basic flow fields with 501 and 251 radial points. Since the difference of the results is in the acceptable level, the number of radial points of the basic flow computation is

appropriate. For the actual stability analysis, the basic flow field was produced with 501 radial points.

6 Results of the Basic Flow Computation

The actual basic flow computation was carried out for air flow over a 4:1 elliptic cone with a 17.5° half angle in the major-axis plane. The Reynolds number per inch was set to 119256; the free-stream Mach number was set to 4; the cone surface was assumed to be of a constant temperature of 531 R. This parameter setup is equivalent to the stagnation pressure of 1 atm and stagnation temperature of 295 K.

Figure 5 shows the pressure distribution on several planes of constant ξ^1 . The inner edge of each plane represents the cone surface while the outer edge represents the bow shock. The computation shows that the distance between the cone surface and the bow shock is smaller on the major axis and near the apex. In Figure 6, the static pressure is plotted on $1/2$ of the unfolded cone surface. It is clearly seen that the pressure is conical and the maximum pressure occurs on the major axis. Because the flow experiences a larger deflection in its flow direction in the major axis region, it is not surprising that the pressure is higher on the major axis. In Figure 7, we can see that the shear stress on the cone surface is greatest on the major axis and near the apex. This is because the velocity just inside the bow shock does not vary much, but the distance between the cone surface and the bow shock is smaller on the major axis and near the apex.

Since the velocity is not uniform inside the boundary layer, the circumferential pressure gradient on the cone surface generates a velocity component normal to the velocity outside the boundary layer. This velocity is called the crossflow velocity whose maximum value in the boundary layer is plotted in Figure 8. It is expected that the maximum crossflow velocities occur in between the major and minor axes because of the symmetry properties of the cone. It can be seen that the maximum crossflow velocity is almost constant on the straight lines originating from the apex which means the maximum crossflow velocity is nearly conical. Since the temperature on the cone surface was assumed to be constant, the density on the cone surface is proportional to the pressure. So the density on the cone surface (shown in Figure 9) has a similar distribution to that of the pressure.

The radial changes of the streamwise, normal, and crossflow velocities, density, temperature, and pressure at $\theta = 72^\circ$ and $\xi^1 = 201.561$ are plotted in Figures 10, 11, 12, 13, 14, and 15. We found that these radial variations of the basic flow variables have similar characteristics at other locations on the cone. According to Rayleigh's theorem, the existence of the inflection point of the basic crossflow velocity u^3 is a necessary condition for the inviscid crossflow instability to occur. From Figure 12, we see that this inflection point does exist. The streamwise variation of the derivative $du^3/d\xi^2$ at the inflection point is shown in Figure 16 for $\theta = 36^\circ$ and 72° . We can see that the magnitude of this derivative is larger near the apex. This is because

the maximum crossflow velocity is almost constant along lines originated from the apex, and the distance between the bow shock and the cone surface is smaller near the apex.

7 Results of the Local Stability Analysis

The search for the unstable crossflow vortex began with the global search at $\xi^1 = 440$. After several trials, α_r was set to 0.03; α_i was set to zero; β was set to 30, which means there are 30 local complete waves in the periphery of the ellipse. ω_r and ω_i were set to be the eigenvalues. Figure 17 shows the distribution of the mode spectrum resulting from the global search. The shape functions of the discrete modes represented in Figure 17 were tested one by one using the local stability analysis. Because the stability characteristics of the flow under consideration are unknown, this procedure had to be used to identify physically relevant instabilities. In Figures 18, 19, 20, 21, and 22, the magnitude and phase of the shape functions of the discrete mode with $\omega_r = 0.000036$ and $\omega_i = 0.001919$ are shown. It should be noted that the magnitude of the velocity in the crossflow direction shown in Figure 20 exhibits some local minima and maxima. This velocity profile also exhibits a phase change of about 180° across the boundary layer. That means that the disturbance velocity in the crossflow direction changes sign in the boundary layer and the the selected mode actually *is* a crossflow vortex. All the other discrete modes do not have this feature. Therefore, further local stability analysis was carried out from this selected mode varying ω_r and ω_i until they were zero. This resulted in a stationary crossflow vortex which was then again verified by checking the magnitude and phase of the shape functions.

After the stationary crossflow vortex was found, the streamwise coordinate ξ^1 was varied for different circumferential locations represented by the angle θ . Figures 23, 24, 25, and 26 show the growth rates for different wavenumbers of the stationary crossflow vortices at $\theta = 36^\circ$, 54° , 72° , and 85.5° . Since the growth rate near the minor (for example, at $\theta = 36^\circ$) and major (for example, $\theta = 85.5^\circ$) axes are smaller than at the angles in between, the crossflow instability weakens toward the symmetry axes and is strongest somewhere in between. This result is consistent with the calculated maximum of the basic crossflow velocity near $\theta = 72^\circ$.

At $\theta = 72^\circ$, the growth rate is larger in the region near the apex. The reason that this can happen is because the derivative of the basic crossflow velocity with respect to ξ^2 at its inflection point (shown in Figure 16) is larger near the apex. This derivative is larger near the apex because the flow is assumed to be conical in the initial plane.

In addition to the stationary crossflow vortex, it is also interesting to look at the stability characteristics of the traveling crossflow vortex with nonzero ω . The streamwise variation of the local growth rate of the traveling crossflow vortex at $\theta = 72^\circ$ with $\omega_r = 0.048$ is shown in Figure 27. This result was predicted from the

linear stability analysis code. By comparing Figure 27 with Figure 25 in which the growth rates of the stationary crossflow vortex were shown, we see that the order of magnitude of the growth rate of the traveling crossflow vortex is about the same as that of the stationary crossflow vortex.

8 Results of the PSE Analysis

To analyze the effects of the nonparallel flow on the stability characteristics of crossflow vortices, PSE analyses were conducted for selected cases previously investigated with the local stability analysis. The solutions from the local stability analysis were used as the input to the PSE code. To ensure that the PSE code generate the results for the same mode, the shape functions of the stationary crossflow vortex generated by the PSE code at a selected location on the cone surface ($\theta = 72^\circ$, $\xi^1 = 100$ and $\beta = 30$) were plotted in Figures 28, 29, 30, 31 and 32. By comparing these figures with Figures 18, 19, 20, 21 and 22, it is seen that the shape functions generated by both the local and PSE analysis are similar. Although only the shape functions at this particular streamwise location are given here, they have been checked for all streamwise locations. Therefore, it is reasonable to believe that they represent the same mode.

Various PSE runs were performed for the stationary crossflow vortices with $\beta = 30, 60$, and 100 at $\theta = 72^\circ$, in the region of strongest crossflow velocity. The streamwise growth rates predicted are given in Figures 33, 34 and 35. The growth rates predicted with the local stability analysis code are also included in those figures for comparison.

The obvious feature of these plots is that the growth rate generated by the PSE is significantly larger than that obtained from the local stability analysis, particularly near the apex. This difference shows that the nonparallel effects are important for the crossflow vortex, particularly near the apex.¹ The reason for the large growth rates in the apex region is that the derivative of the crossflow velocity with respect to the radial coordinate at the inflection point is large. By comparing the PSE generated growth rates for $\beta = 30, 60$ and 100 , we found that the stationary crossflow vortex is most unstable at $\beta = 60$.

The results of a $N (= -\int \alpha_i d\xi^1)$ factor analysis for these same cases are shown in Figure 36. The PSE analysis predicts that the crossflow causes transition to occur at about $\xi = 150$ (1.1 in.) while the local stability analysis code predicts transition will not be caused by crossflow vortices.

¹We have observed similar large effects of nonparallel terms on crossflow vortices in the leading edge region of swept wings with rapid changes of curvature.

9 Conclusion

The basic flow for a 4:1 elliptic cone with 17.5° half angle on the major axes has been computed and documented for a Mach number of 4. Both the local stability and PSE analyses were performed for this basic flow. The analyses reveal the existence of both stationary and traveling crossflow vortices. At a fixed axial location, the crossflow instability is strongest in the region near 72° from the minor axis. At a fixed circumferential position, such as at 72° from the minor axis, the growth rate of the crossflow vortex is largest in the region near the apex. The crossflow vortices are associated with the existence of an inflection point in the the crossflow velocity which is normal to the boundary layer edge velocity. The reason for the large growth rate near the apex is the large derivative of the crossflow velocity with respect to the radial coordinate at the inflection point.

The nonparallel effects on the stability characteristics were found important. To correctly address the growth problem of the crossflow vortices, the nonparallel effects must be included.

According to the e^N analysis, the stationary crossflow vortex with $\beta = 60$ initiates transition at $\xi = 1.1$ inches and $\theta = 72^\circ$ if $N = 10$ is assumed in absence of any empirical data. Our result is opposite to the findings of Lyttle (1994) who used transition correlations for the same configuration. Although the azimuthal variations of the basic flow had to be neglected in our analysis, we believe that the stability characteristics of the three-dimensional flow are sufficiently approximated by our results to warrant manufacturing of the configuration for experimental study.

10 Appendix A: Reference Data and Conversions

Dimensional quantities are denoted by a superscript star (*). The fluid is standard air.

Mach number	$M = 4$		
Prandtl number	$Pr = 0.72$		
Freestream:			
Stagn. Temperature	T_0^*	$295K$	$531R$
Stagn. Pressure	P_0^*	$1.01352 \cdot 10^5 N/m^2$	$2116.8 lb_f/ft^2$
Static Temperature	T_∞^*	$70.24K$	$126.43R$
Static Pressure	P_∞^*	$667.55 N/m^2$	$13.942 lb_f/ft^2$
Velocity	$V_\infty^* = M\sqrt{kRT}$	$671.98 m/s$	$2204 ft/s$
Length of cone axis	L^*	$0.1524 m$	$0.5 ft$
Length scale	$\delta^* = \sqrt{\nu_\infty L/V_\infty}$	$1.87034 \cdot 10^{-4} m$	$7.3635 \cdot 10^{-3} in$
Time scale	$\tau^* = L/V_\infty$	$2.2679 \cdot 10^{-4} s$	
Conversions:			
Velocities	$u_i^* = u_i V_\infty$	m/s	ft/s
Coordinate (Fig. 1)	$\xi_1^* = \xi_1 \delta^*$	m	ft
Coordinate (Fig. 1)	$\xi_2^* = \xi_2 \delta^*$	m	ft
Coordinate (Fig. 1)	$\xi_3^* = \xi_3$	rad	
	$T^* = TT_\infty^*$	K	R
	$P^* = PP_\infty^*$	N/m^2	lb_f/ft^2
	$\omega^* = \omega/\tau^*$	$1/s$	
	$\alpha^* = \alpha/\delta^*$	$1/m$	$1/ft$
	$\beta^* = \beta$	$1/rad$	
Total wave number	$k^* = \sqrt{\alpha^{*2} + (\frac{\beta^*}{r^*})^2}$	$1/m$	$1/ft$
Wave length	$\lambda^* = 1/k^*$	m	ft
Local body radius	r^*	m	ft

11 References

Aeschliman, D. P. 1992 "Liquid Crystals Reveal Flow Patterns at Higher Supersonic Speeds," Testing Technology, Sandia National Laboratories, Sept. 1992, pp. 7-8.

Arnal, D., Vignau, F., and Laburthe, F. 1991 "Recent Supersonic Transition Studies with Emphasis on the Swept Cylinder Case," In: Proc. Conf. on Boundary Layer Transition and Control, 8-12 April 1991, Cambridge, UK.

Demetriades, A. 1977 "Laminar Boundary Layer Stability Measurements at Mach 7 Including Wall Temperature Effects," AFOSR-TR-77-1311.

Herbert, Th. and Esfahanian, V. 1993 "Stability of hypersonic flow over a blunt body," In: *Theoretical and Experimental Methods in Hypersonic Flows*, AGARD CP 514, Paper 28.

Herbert, Th. 1993 "Parabolized Stability Equations," AGARD R-793, Madrid, Spain, 22-25, March 1993.

Herbert, Th., Stuckert, G. K., Lin, N. 1993 "Method for Transition Prediction in High Speed Boundary Layers," WL-TR-93-3097, Sept. 1993

Kendall, J. M. 1975 "Wind Tunnel Experiments Relating to Supersonic and Hypersonic Boundary-Layer Transition," AIAA J., Vol. 13, pp. 240-299.

Lyttle, I. J. 1994 "On the Use of Transition Correlations for Three-Dimensional Boundary Layers within Hypersonic Viscous Flows," M.S. Thesis, Arizona State University, Tempe, Arizona.

Mack, L. M. 1984 "Boundary-layer linear stability theory," AGARD Report No. 709, Paper 3.

Mack, L. M. 1986 "Boundary-layer stability analysis for sharp cones at zero angle of attack," AFWAL TR-86-3022.

Malik, M. R., Spall, R., and Chang, C. 1990 "Effect of nose bluntness on boundary layer stability and transition," AIAA Paper No. 90-0112.

Oberkampf, W. L. and Aeschliman, D. P. 1992 "Joint Computational/Experimental Aerodynamics Research on a Hypersonic Vehicle, Part 1: Experimental Results," AIAA J., Vol. 30, pp. 2000-2009.

Ramakrishnan, R., Vatsa, V., Otto, J., and Kumar, A. 1993 "A Detailed Study of Mean-Flow Solution for Stability Analysis of Transitional Flows," AIAA 93-3052.

Smith, A. M. D. and Gamberoni, A. H. 1956 "Transition, Pressure Gradients and Suction," AGARD CP-224, Paper No. 6.

Stalnaker, J. F., Nicholson, L. A., Hanline, D. S. and McGraw, E. H. 1986 "Improvements to the AFWAL parabolized Navier-Stokes Code Formulation," AFWAL-TR-86-3076, Sept. 1986.

Stetson, K. F., Thompson, E. R. and Donaldson. J. C. 1983 "Laminar boundary layer stability experiments on a cone at Mach 8, Part 1: Sharp cone," AIAA Paper No. 83-1761.

Stetson, K. F., Thompson, E. R., Donaldson. J. C. and Siler, L. G. 1985 "Laminar boundary layer stability experiments on a cone at Mach 8, Part 2: Blunt cone," AIAA Paper No. 84-0492.

12 Figures

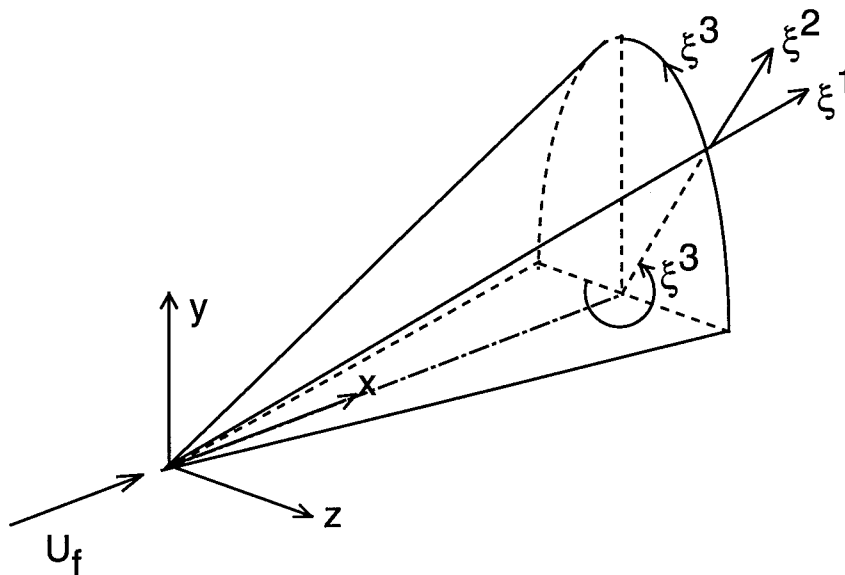


Figure 1: Coordinate system.

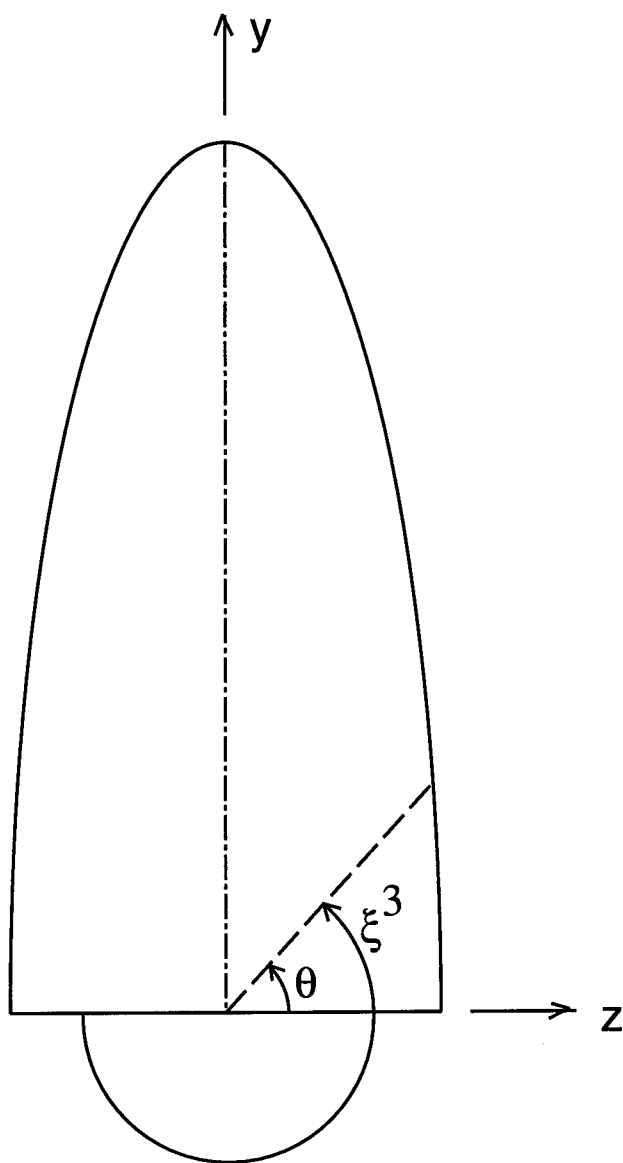


Figure 2: A Cross-section of the 4:1 elliptic cone.

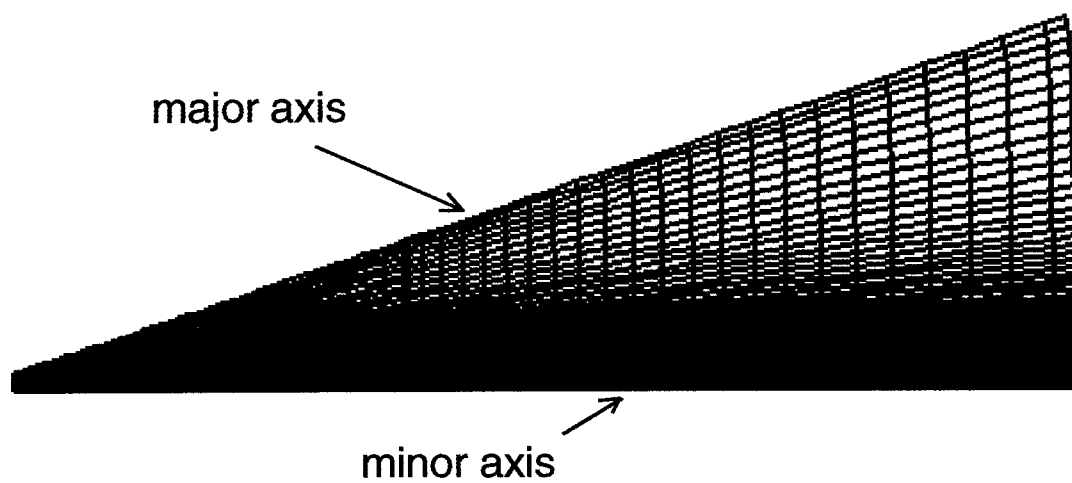


Figure 3: Basic flow computational grid on the unfolded cone surface (vertical grid lines are output every 4 grid lines).

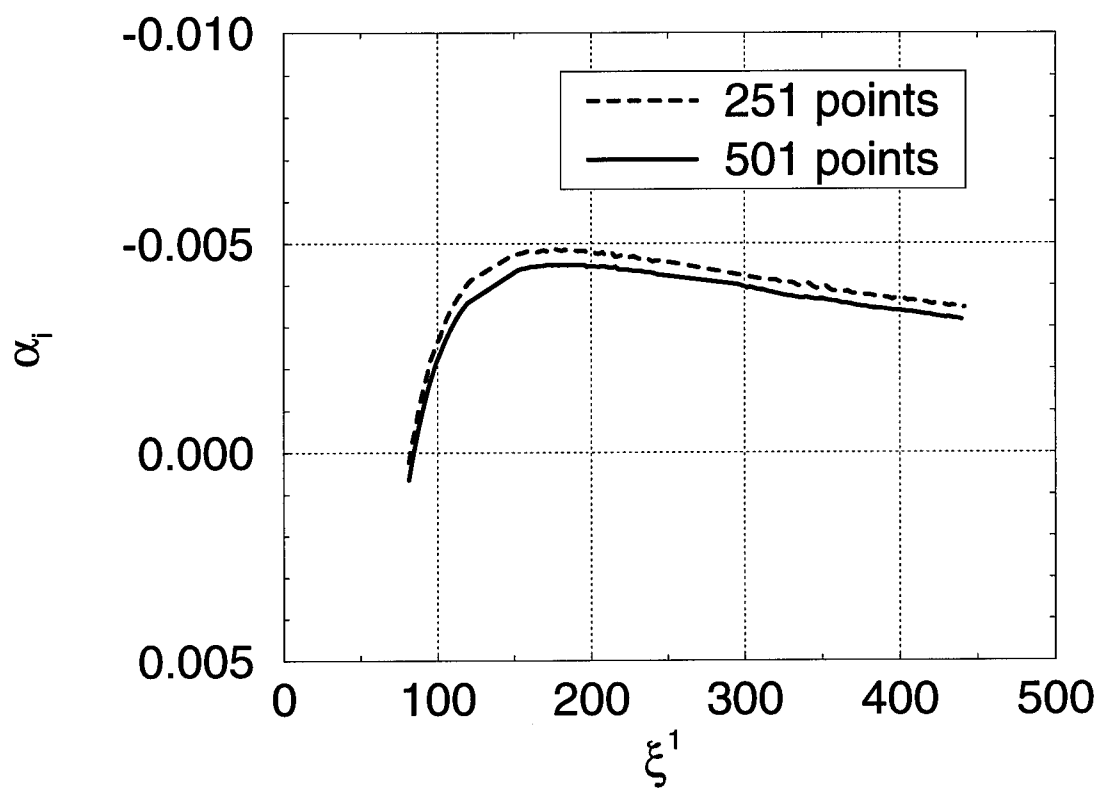


Figure 4: Effect of different numbers of points in radial direction.

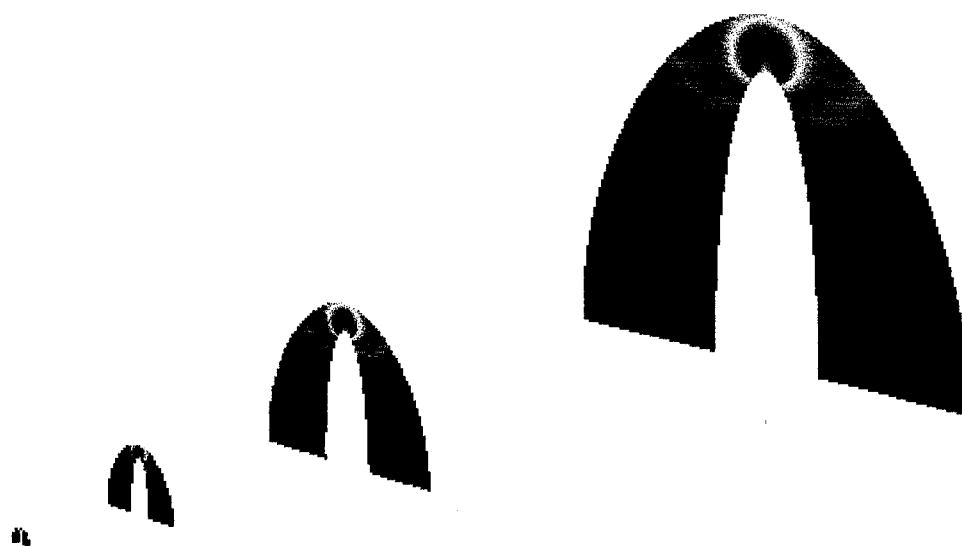


Figure 5: Pressure distribution on several planes in streamwise direction.



Figure 6: Pressure distribution on the unfolded cone surface.



Figure 7: Shear stress distribution on the unfolded cone surface.

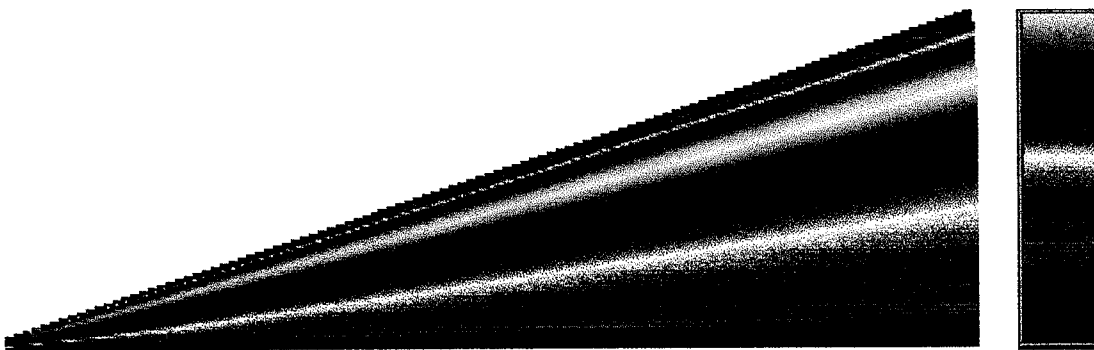


Figure 8: Maximum crossflow velocity distribution on the unfolded cone surface.



Figure 9: Density distribution on the unfolded cone surface.

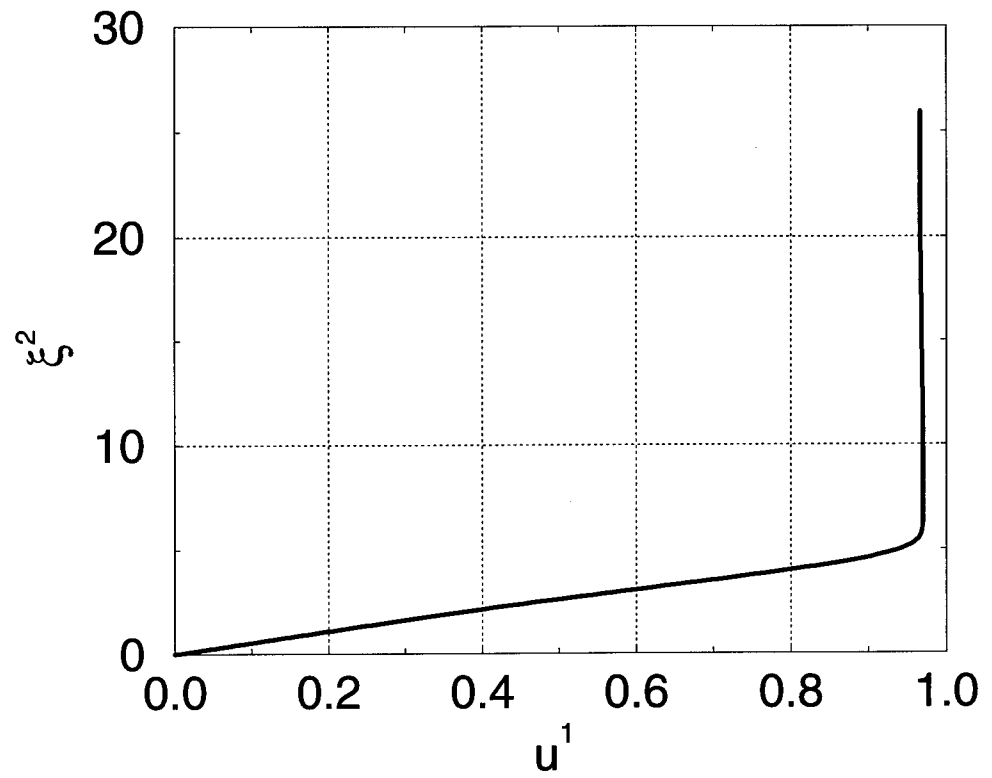


Figure 10: Distribution of the basic velocity component in the direction of the boundary layer edge velocity (streamwise velocity) at $\theta = 72^\circ$ and $\xi^1 = 201.561$.

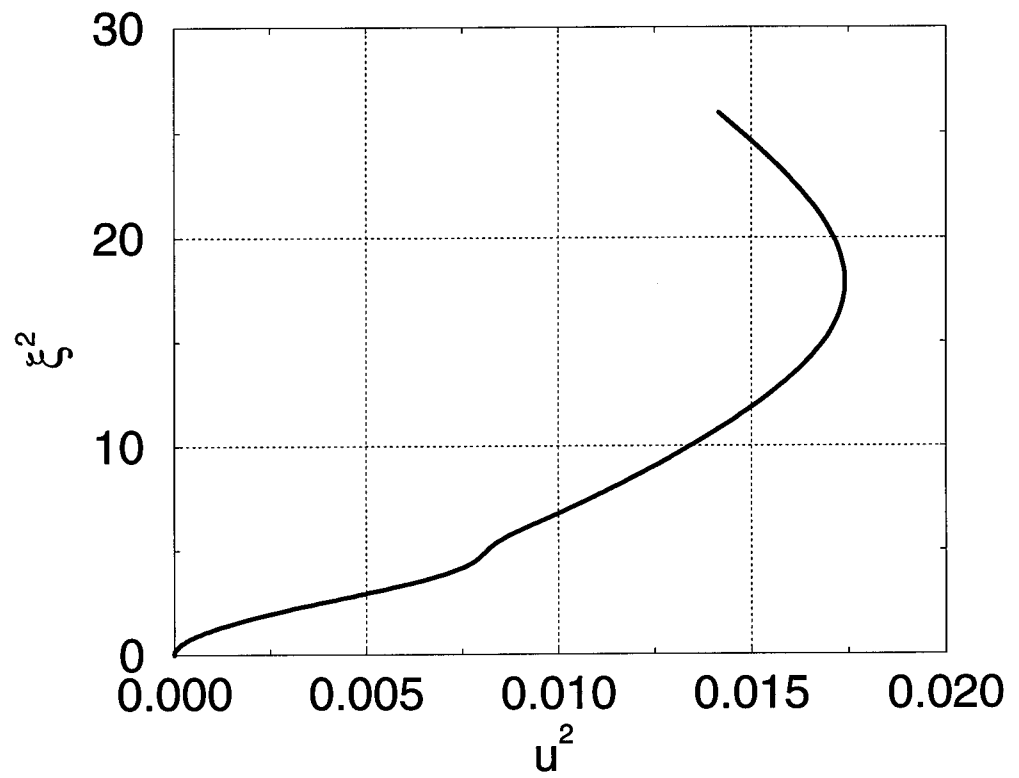


Figure 11: Distribution of the basic ξ^2 velocity component (radial velocity) at $\theta = 72^\circ$ and $\xi^1 = 201.561$.

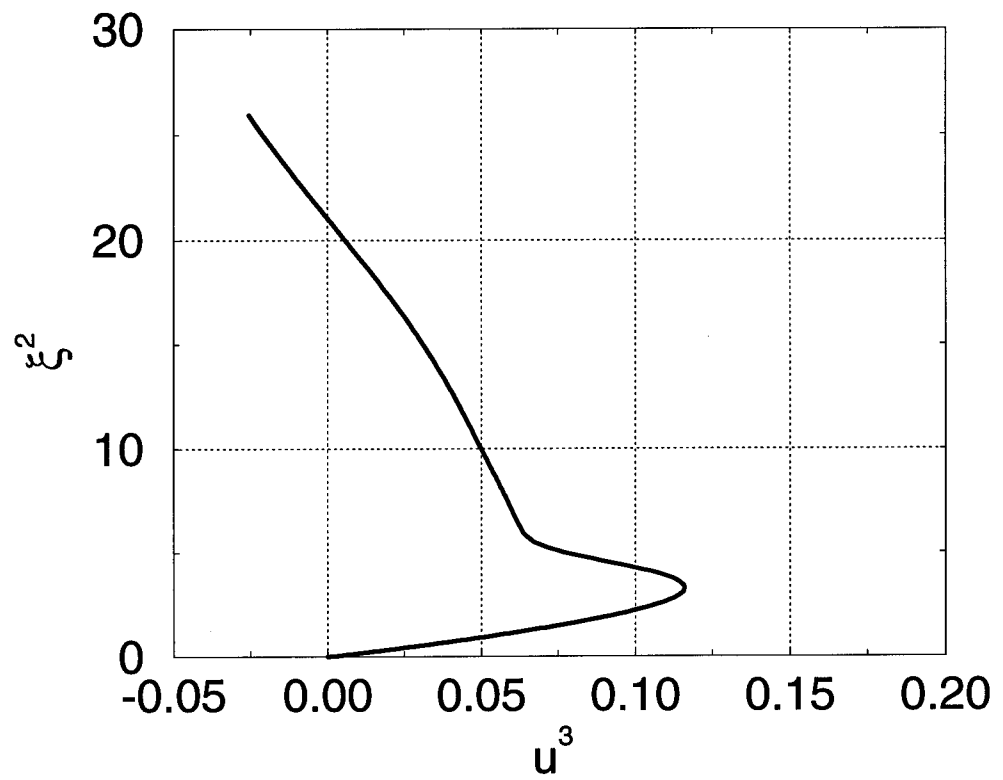


Figure 12: Distribution of the basic velocity component normal to the direction of the boundary layer edge velocity (crossflow velocity) at $\theta = 72^\circ$ and $\xi^1 = 201.561$.

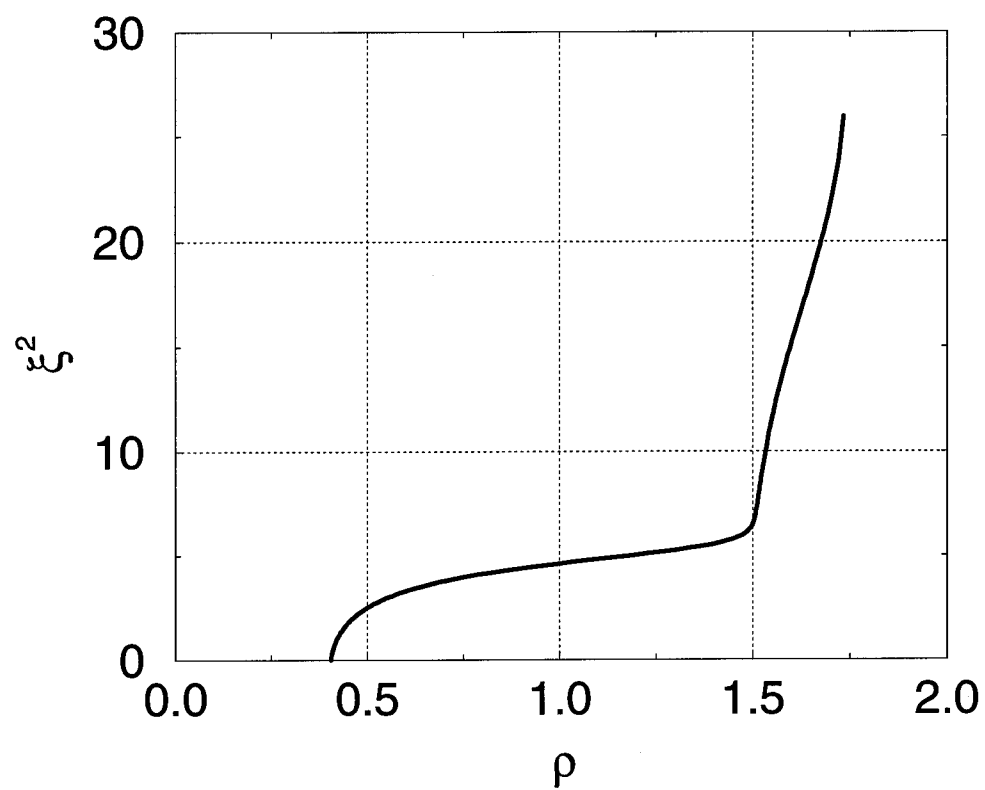


Figure 13: Distribution of the basic density at $\theta = 72^\circ$ and $\xi^1 = 201.561$.

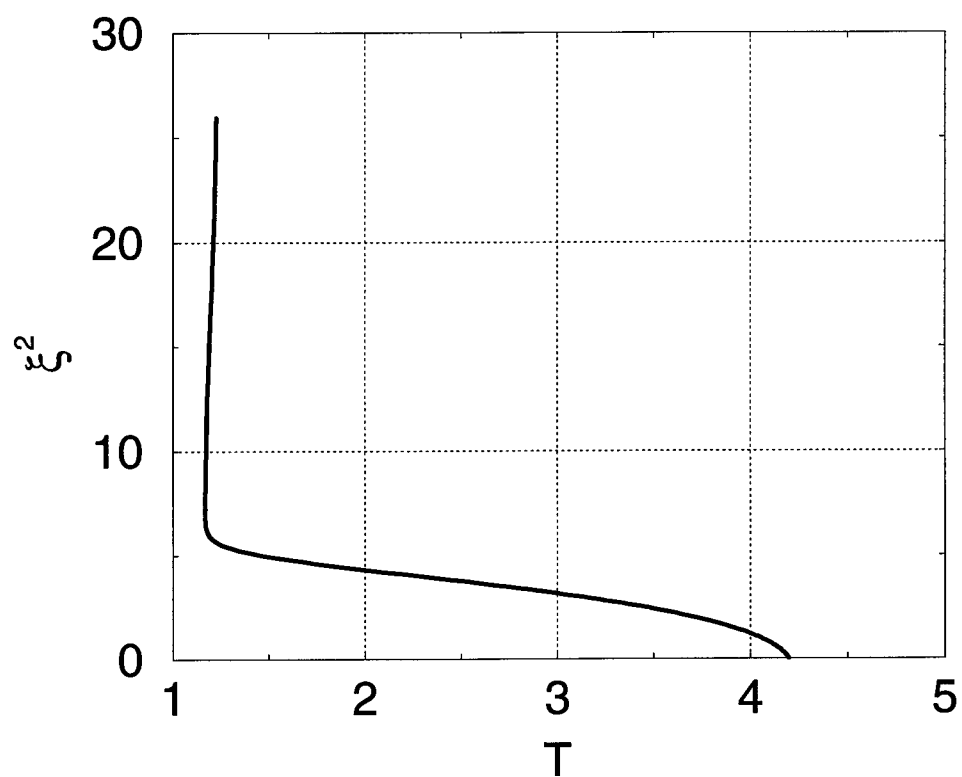


Figure 14: Distribution of basic temperature at $\theta = 72^\circ$ and $\xi^1 = 201.561$.

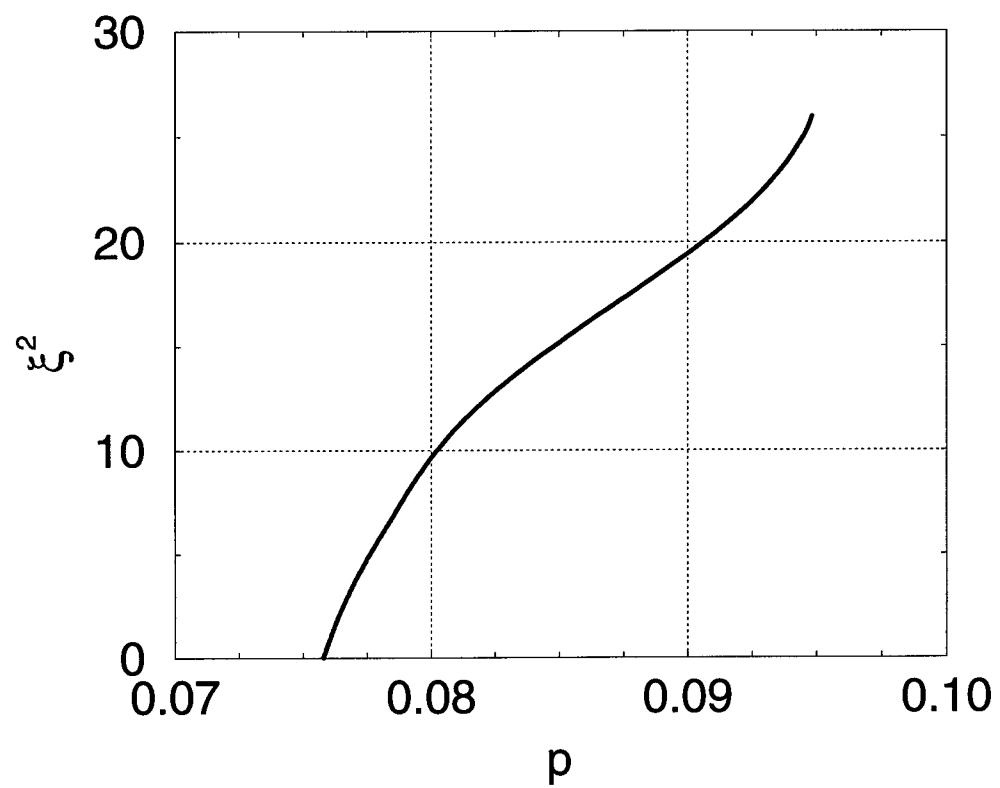


Figure 15: Distribution of the basic pressure at $\theta = 72^\circ$ and $\xi^1 = 201.561$.

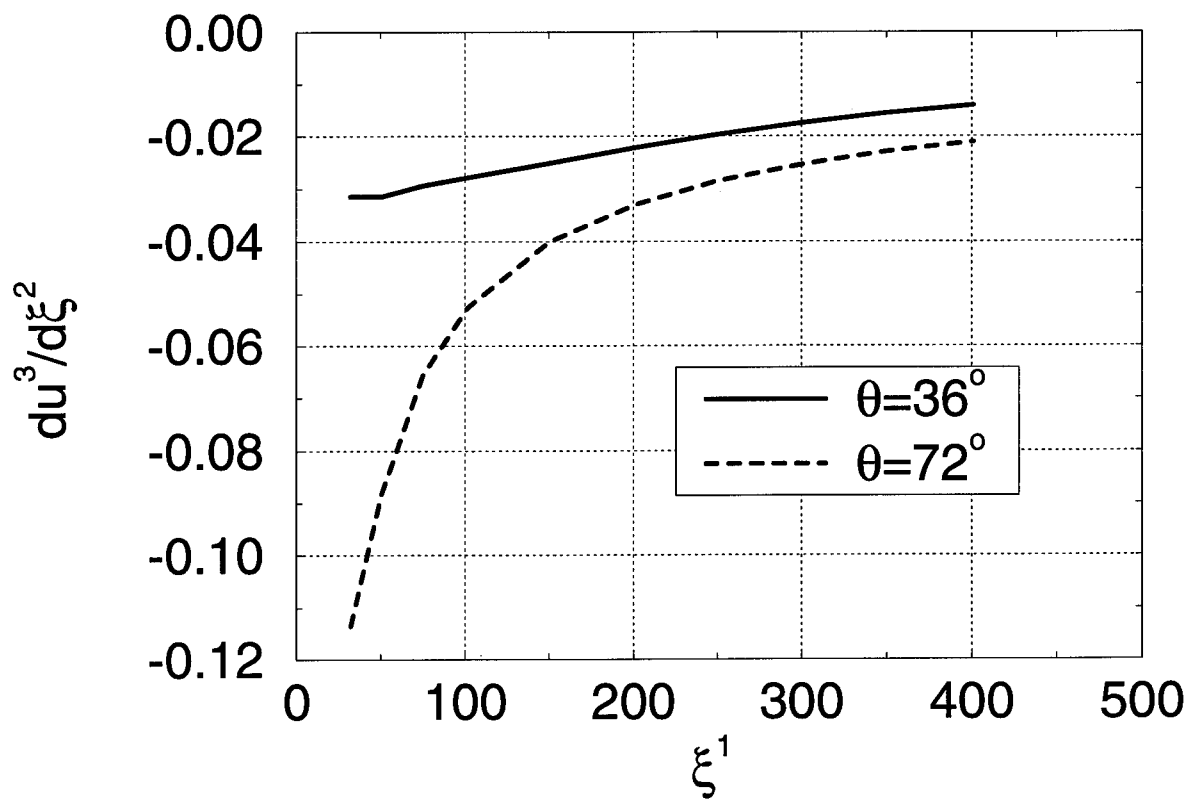


Figure 16: Derivative of the crossflow velocity with respect to ξ^2 at the inflection point at $\theta = 36^\circ$ and $\theta = 72^\circ$.

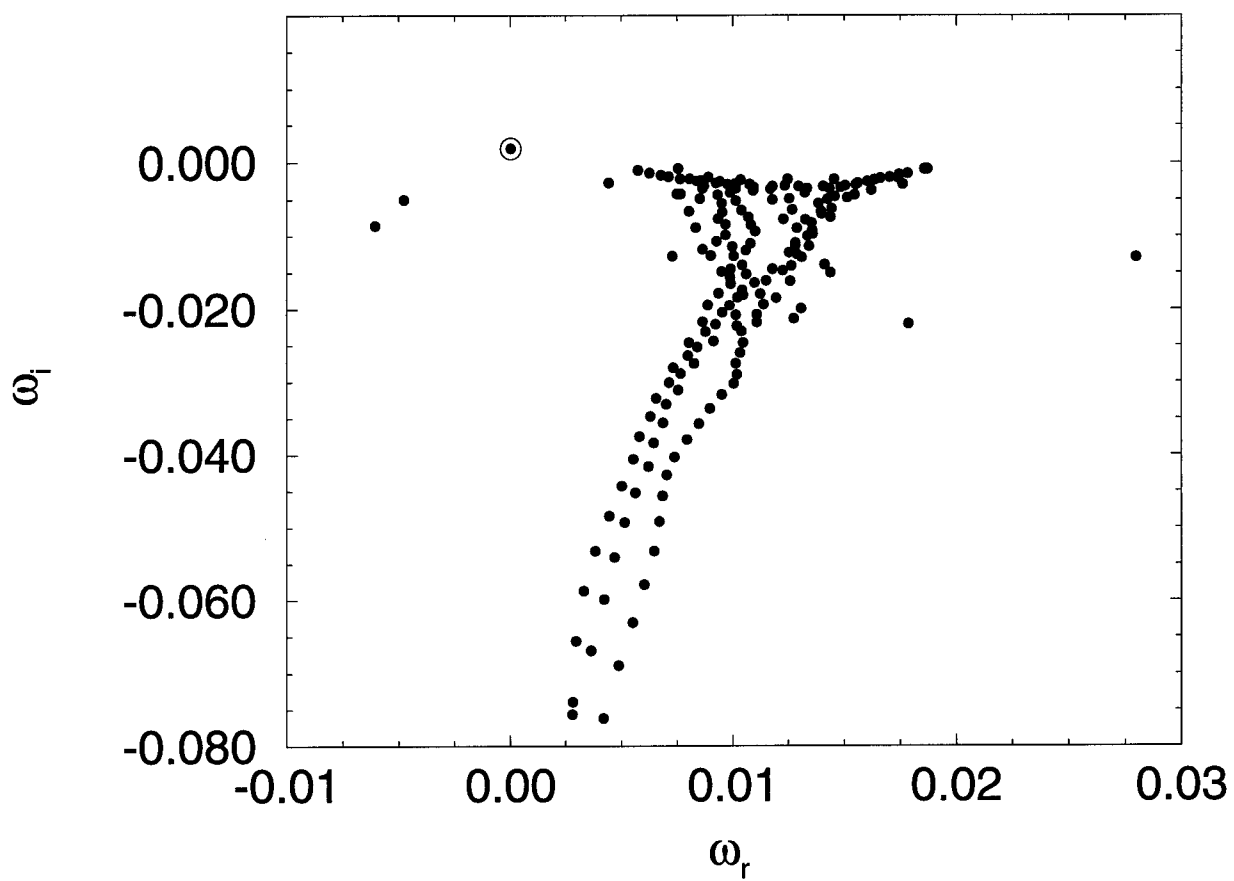


Figure 17: Spectrum of the instability modes. The dominant crossflow mode is enclosed in a circle.

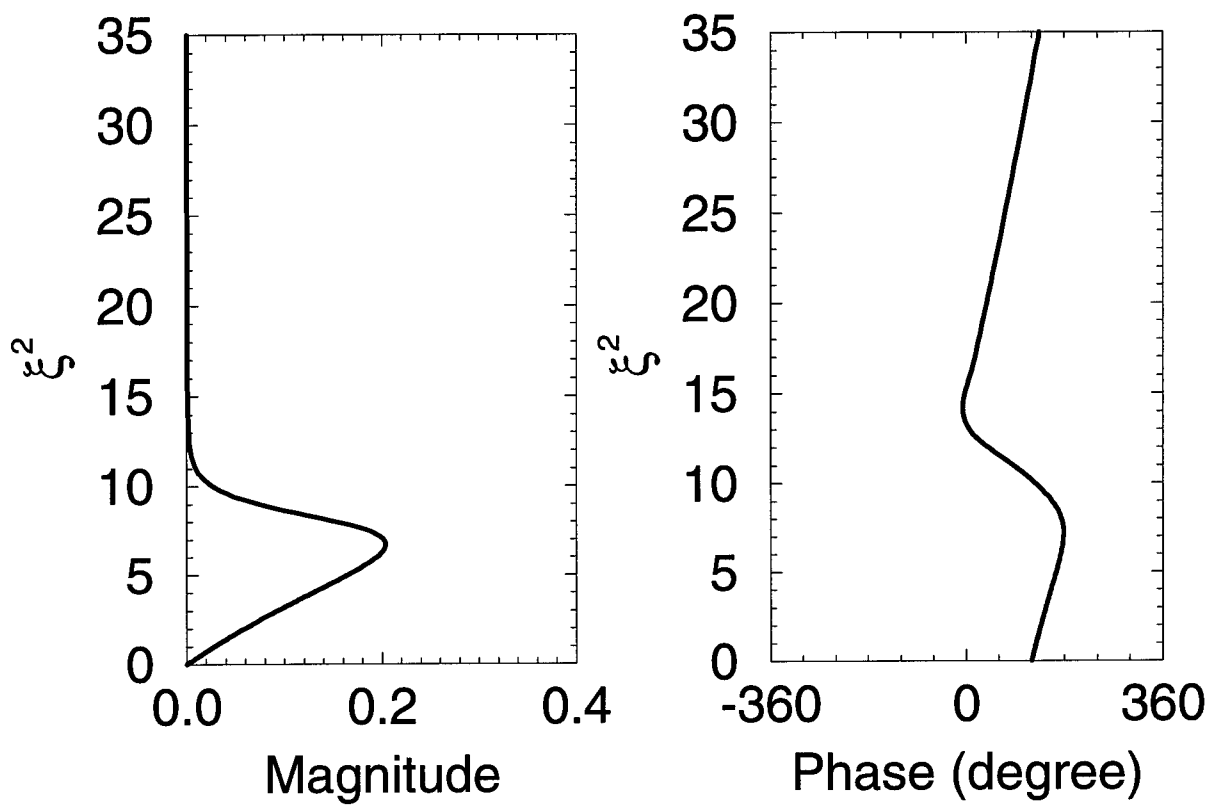


Figure 18: Magnitude and phase of the streamwise velocity shape function u_1 .

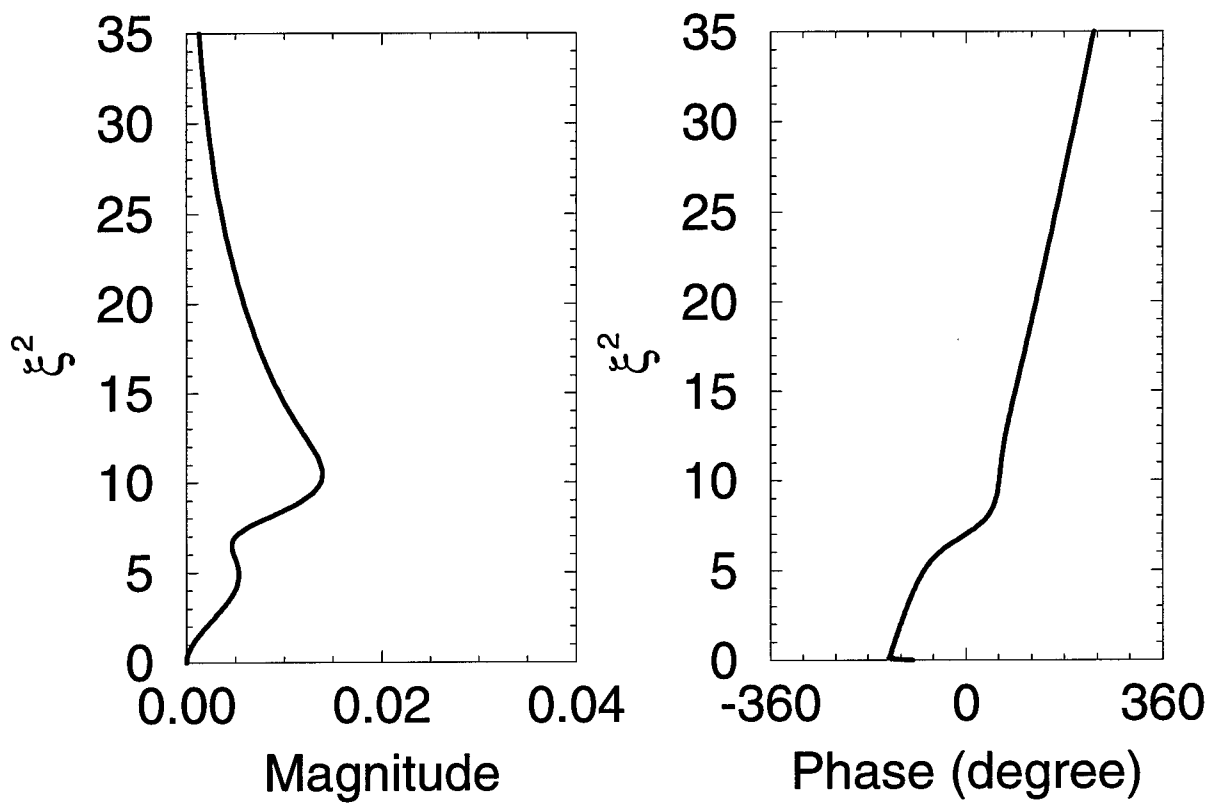


Figure 19: Magnitude and phase of the radial velocity shape function u_2 .

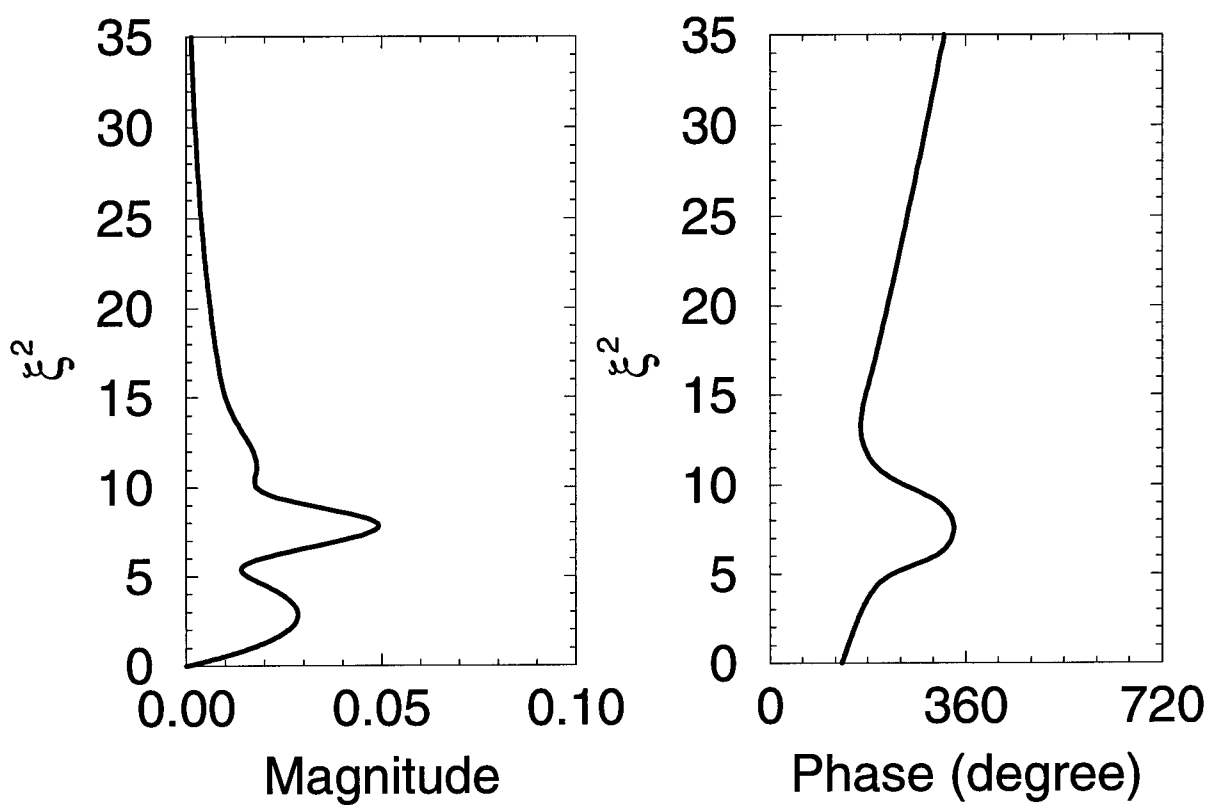


Figure 20: Magnitude and phase of the velocity shape function u_3 in the crossflow direction.

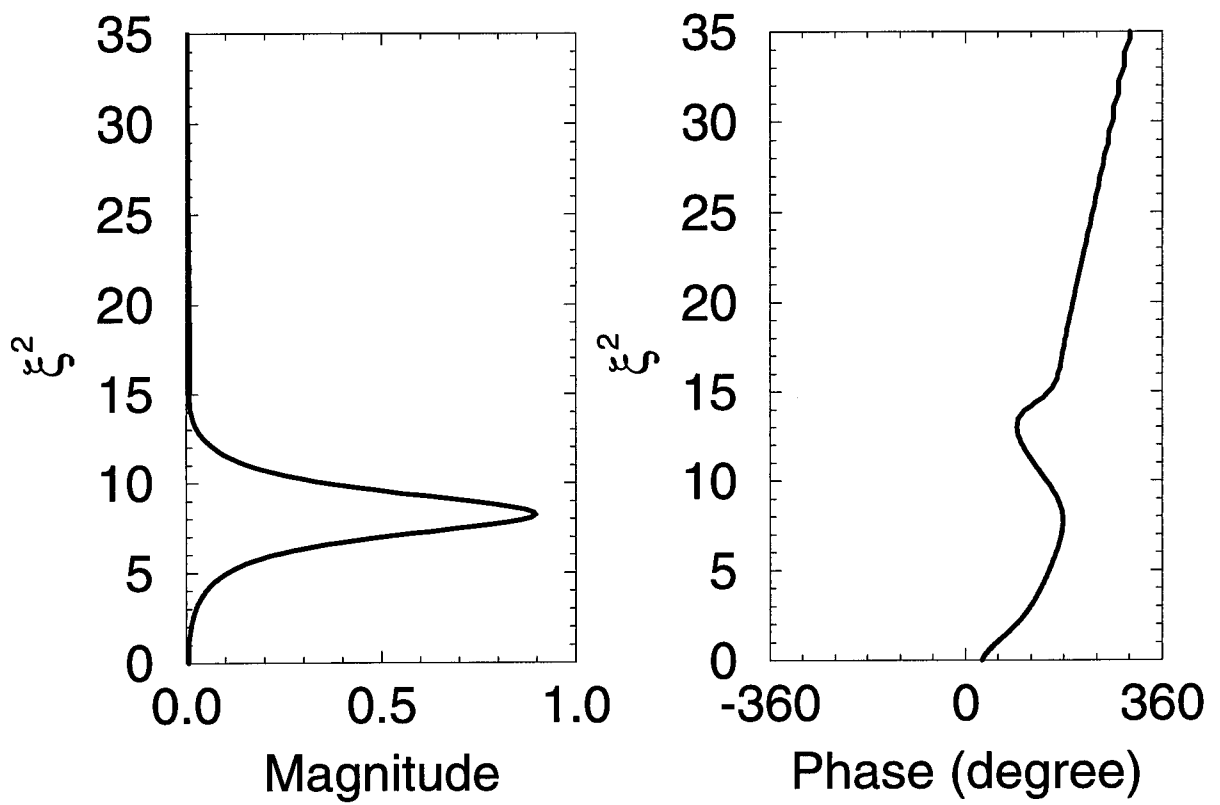


Figure 21: Magnitude and phase of the density shape function.

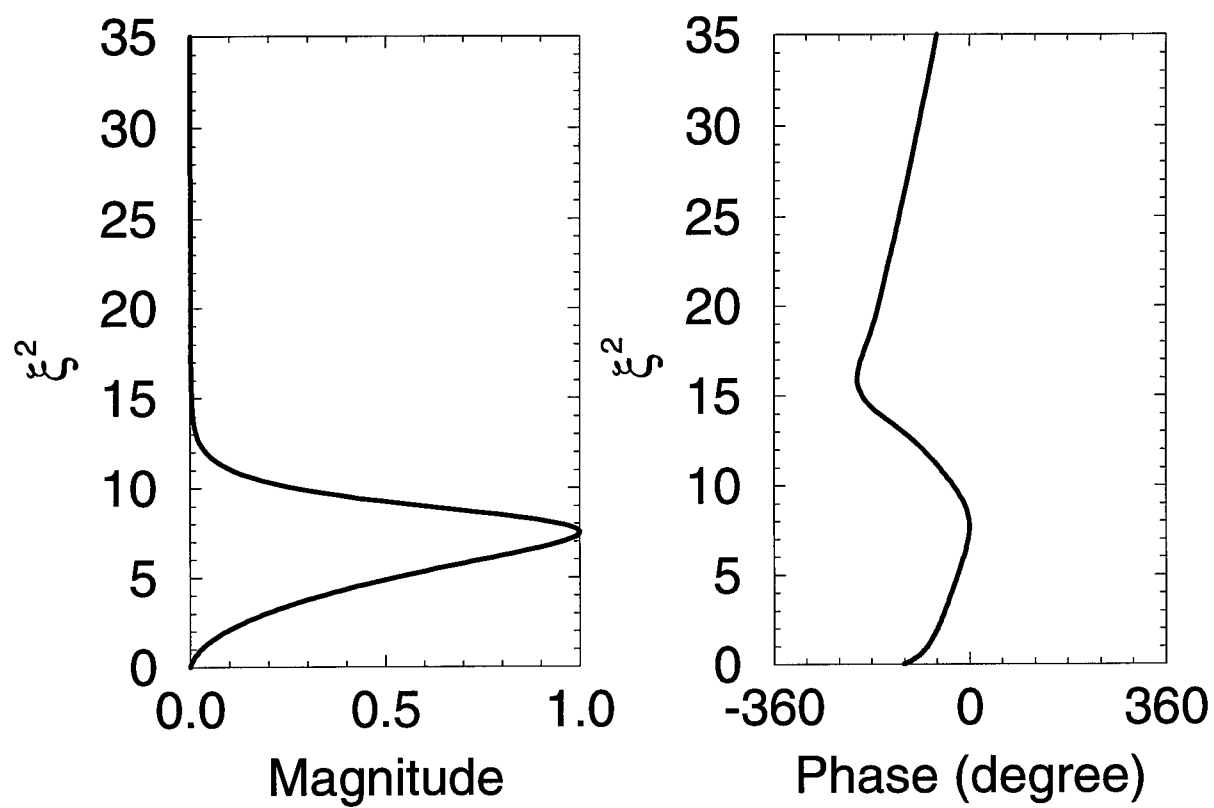


Figure 22: Magnitude and phase of the temperature shape function.

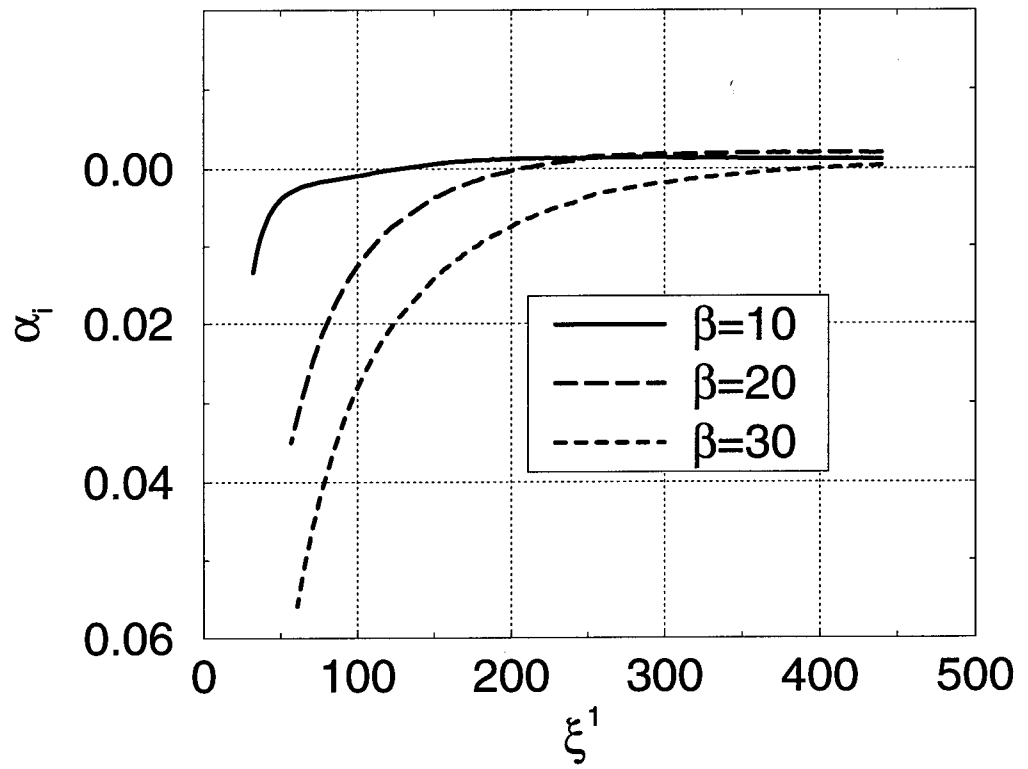


Figure 23: Local growth rate of the stationary crossflow vortex at $\theta = 36^\circ$.

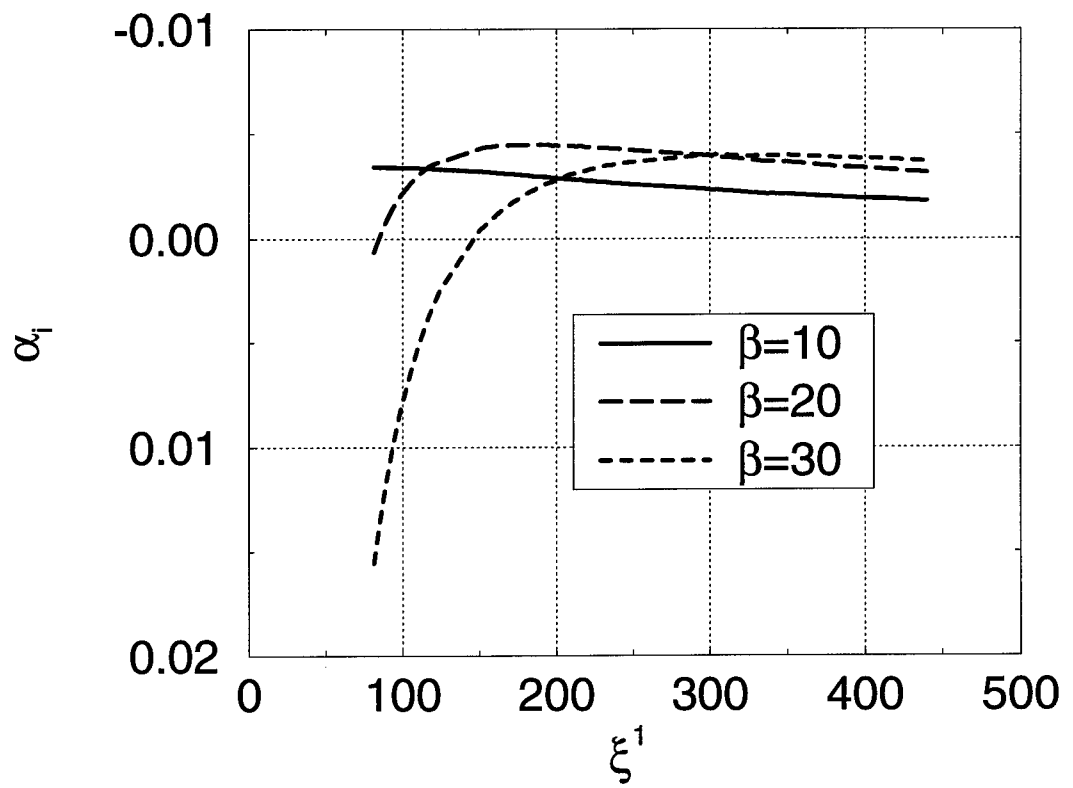


Figure 24: Local growth rate of the stationary crossflow vortex at $\theta = 54^\circ$.

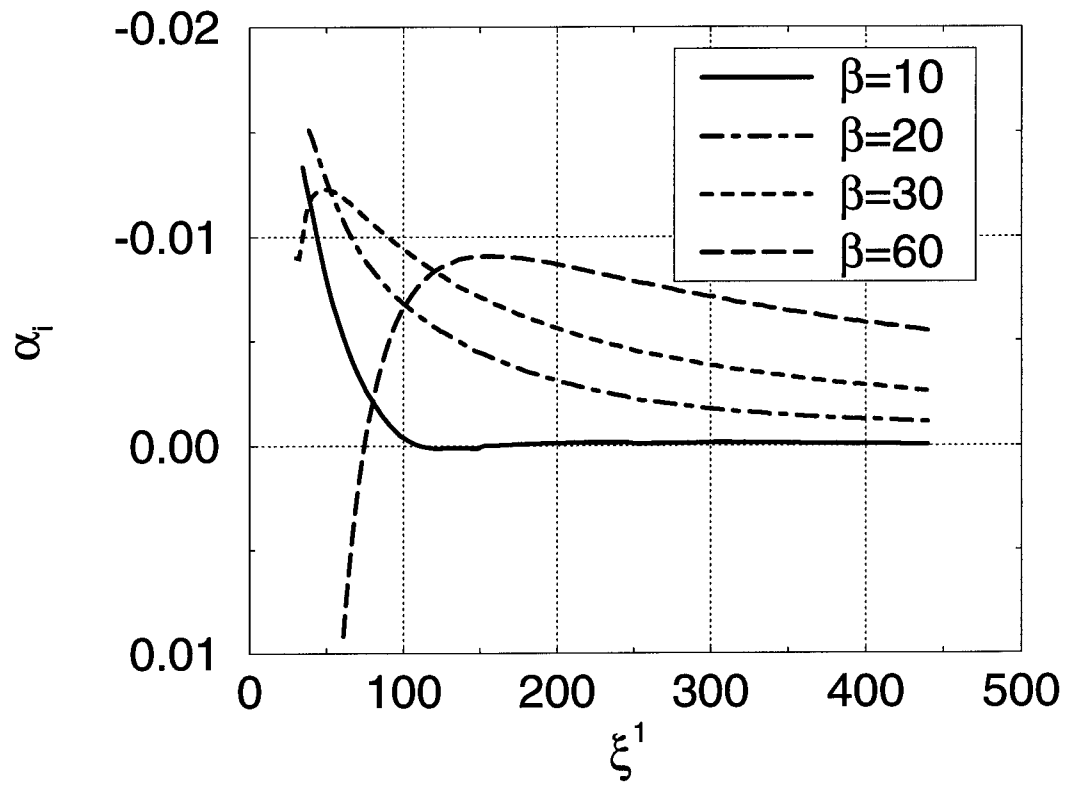


Figure 25: Local growth rate of the stationary crossflow vortex at $\theta = 72^\circ$.

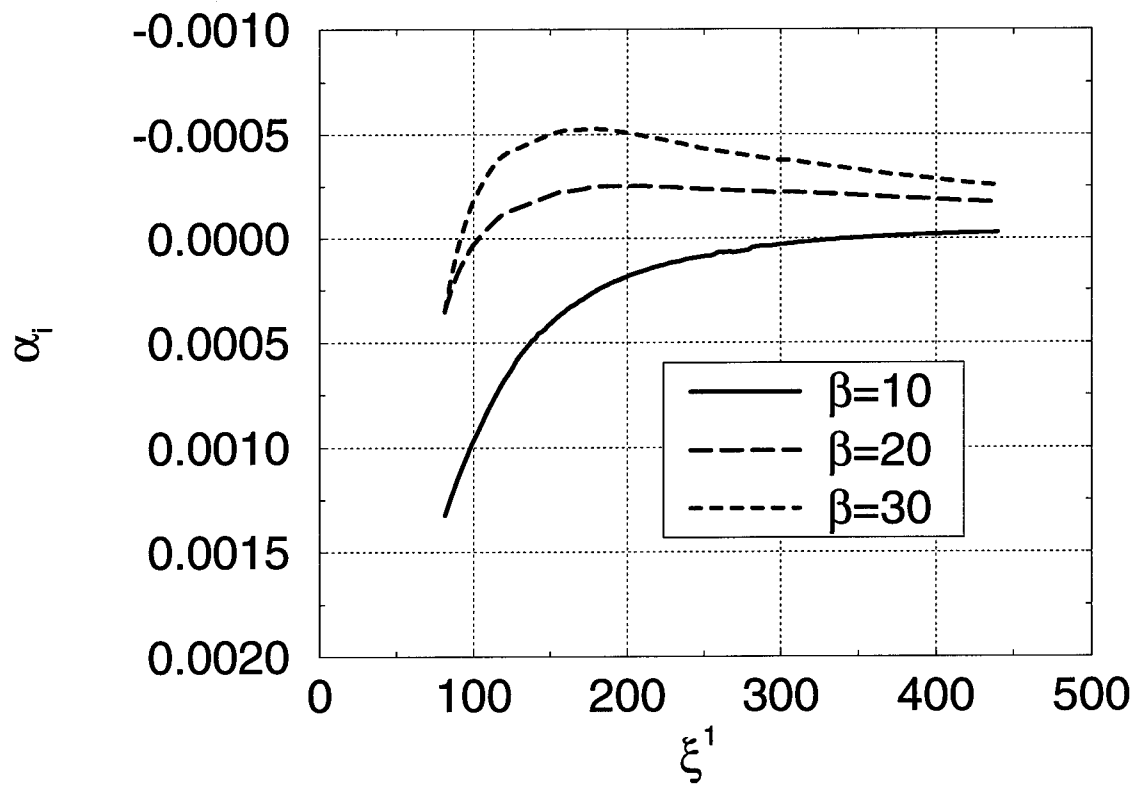


Figure 26: Local growth rate of the stationary crossflow vortex at $\theta = 85.5^\circ$.

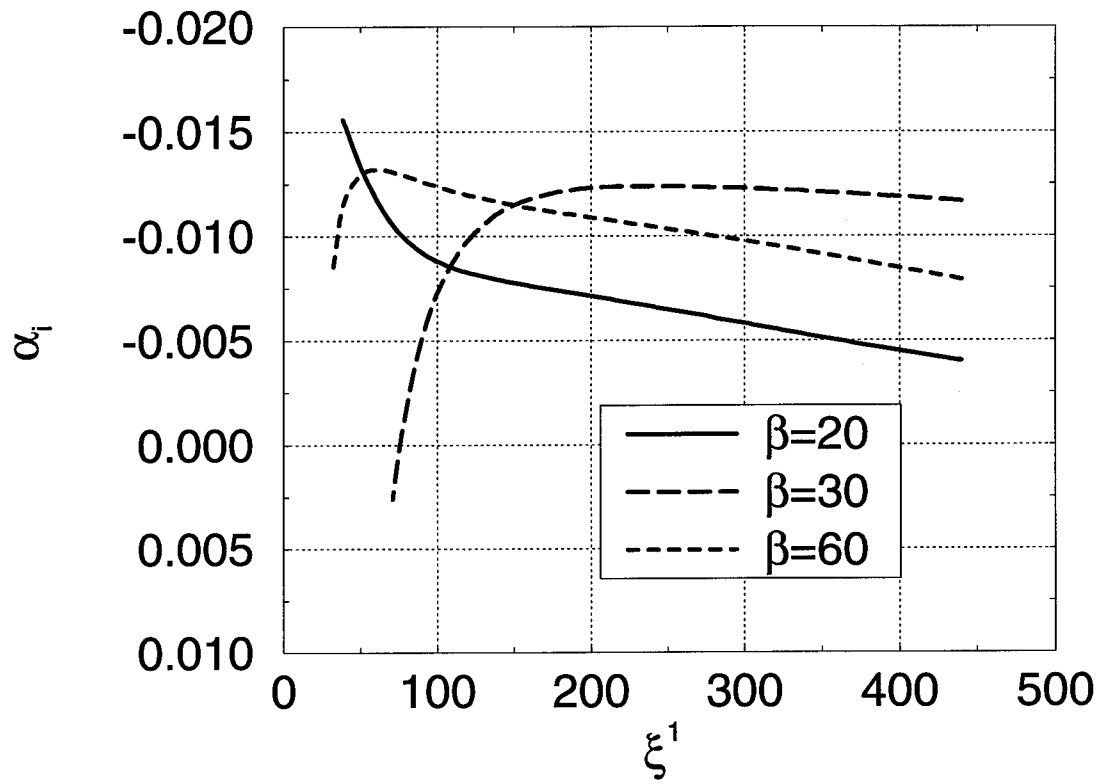


Figure 27: Local growth rate of the traveling crossflow vortex ($\omega_r = 48$) at $\theta = 72^\circ$.

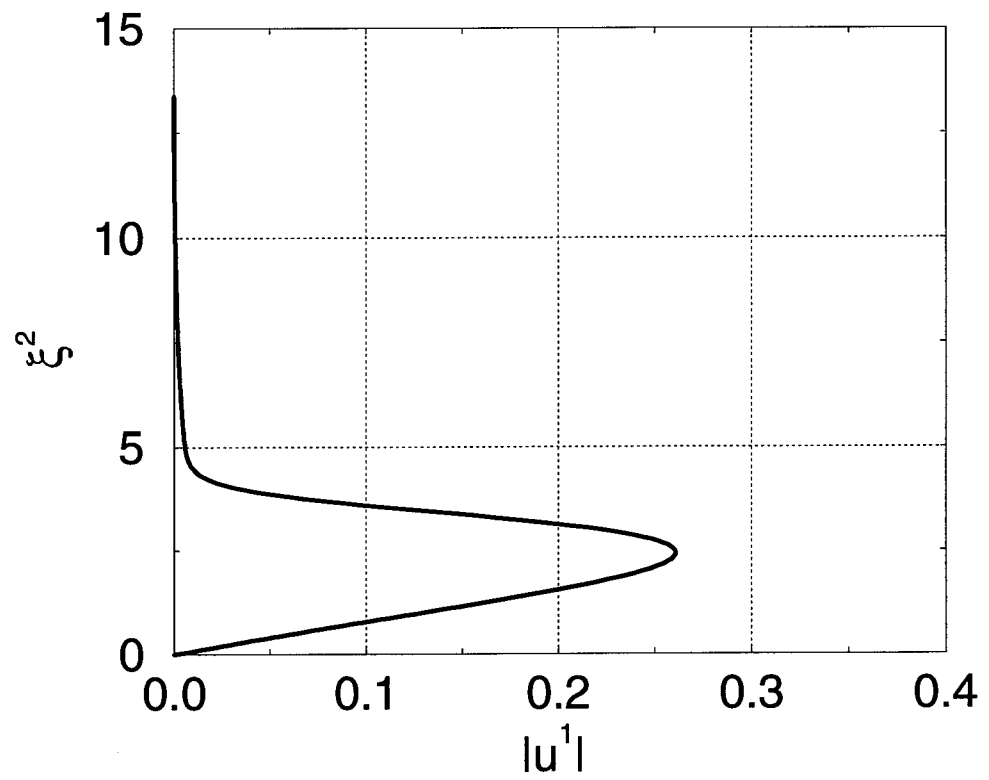


Figure 28: PSE result for the streamwise velocity shape function of the stationary crossflow vortex at $\theta = 72^\circ$ and $\beta = 30$.

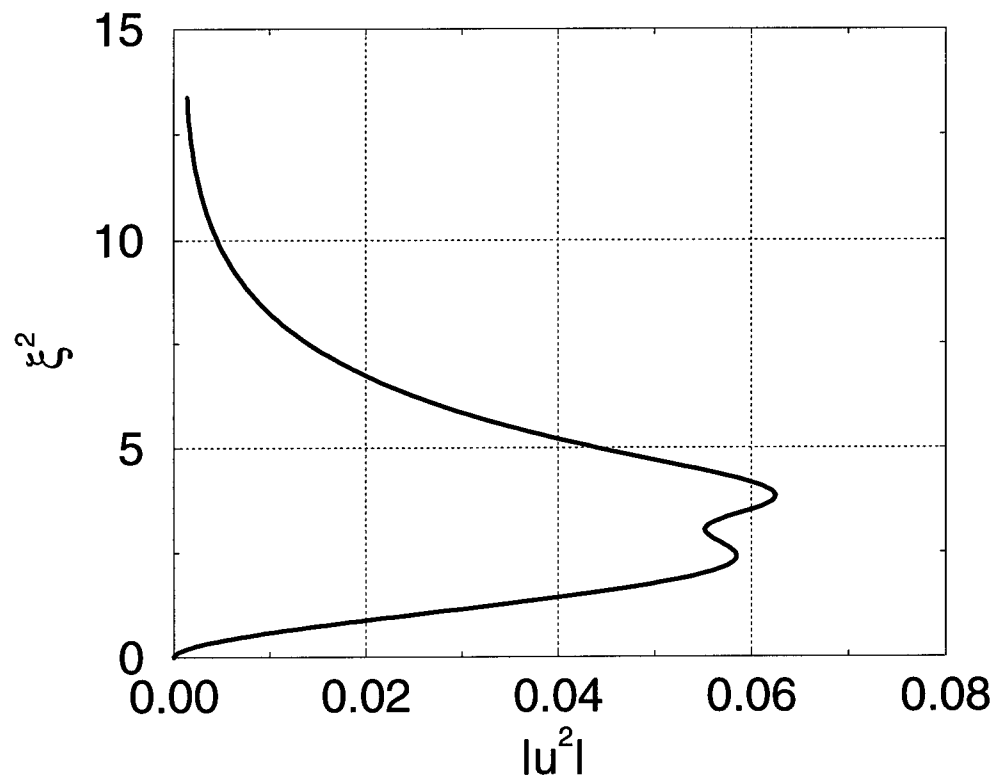


Figure 29: PSE result for the radial velocity shape function of the stationary crossflow vortex at $\theta = 72^\circ$ and $\beta = 30$.

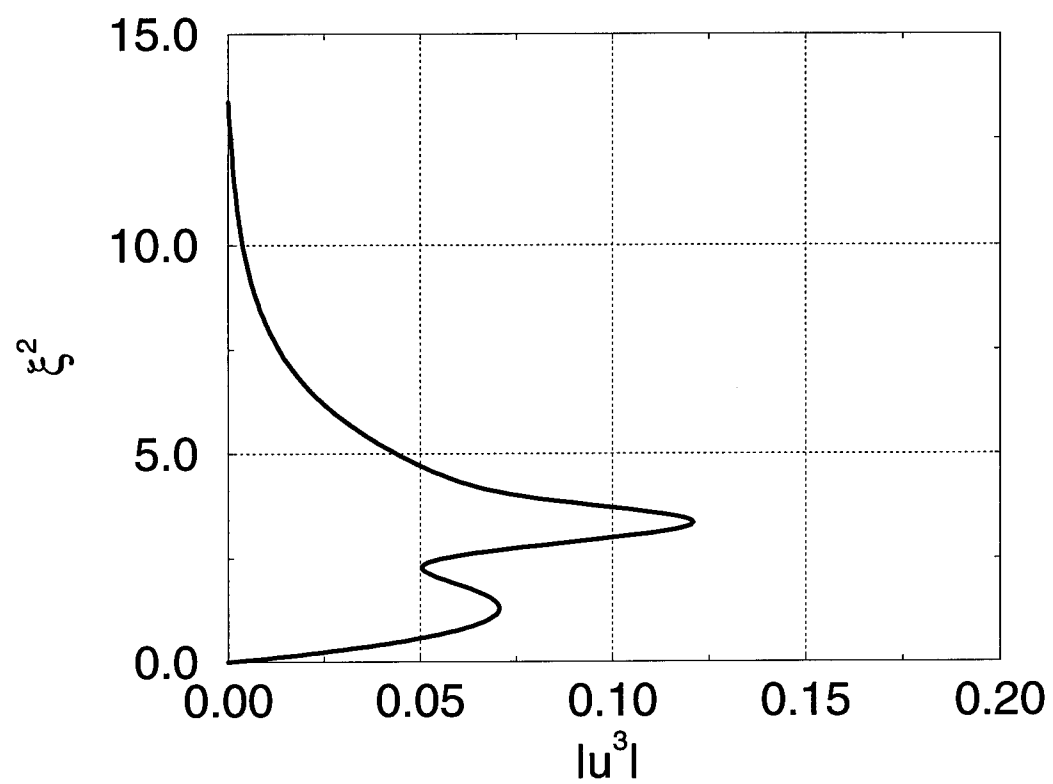


Figure 30: PSE result for the crossflow velocity shape function of the stationary crossflow vortex at $\theta = 72^\circ$ and $\beta = 30$.

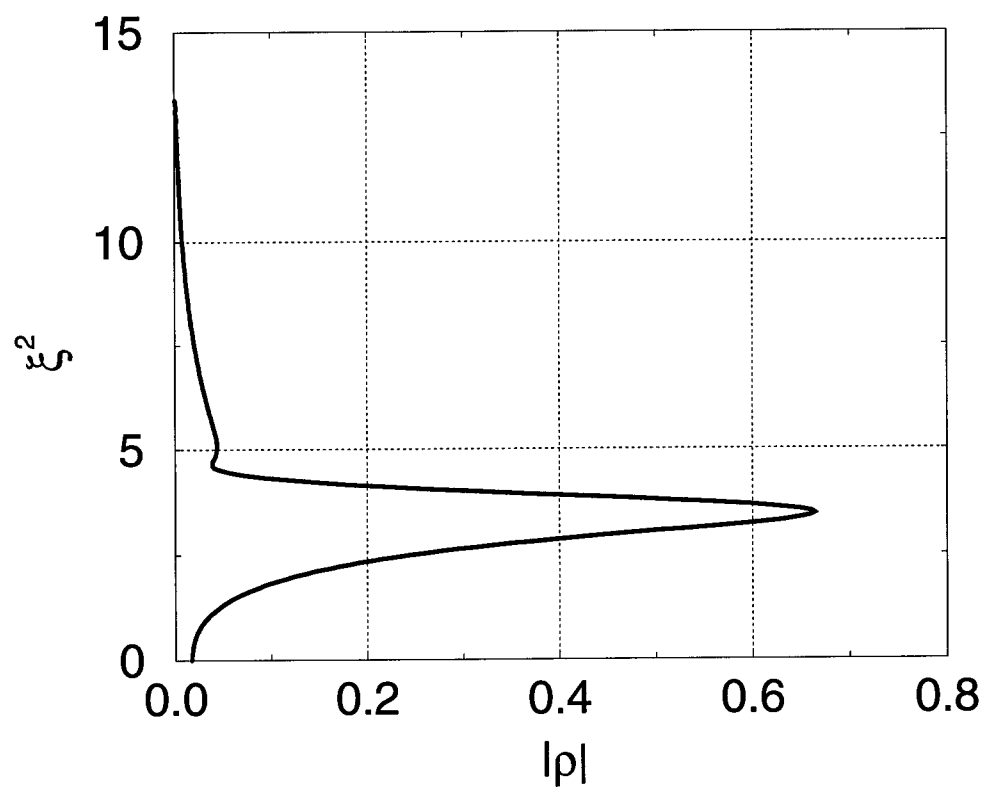


Figure 31: PSE result for the density shape function of the stationary crossflow vortex at $\theta = 72^\circ$ and $\beta = 30$.

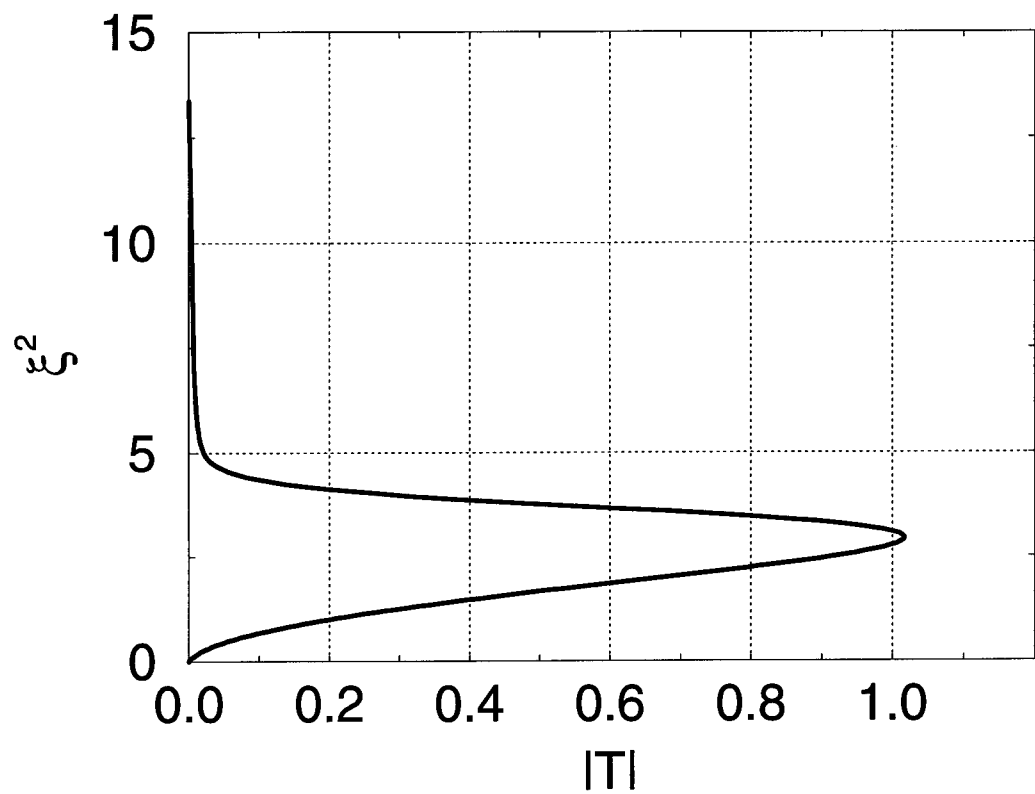


Figure 32: PSE result for the temperature shape function of the stationary crossflow vortex at $\theta = 72^\circ$ and $\beta = 30$.

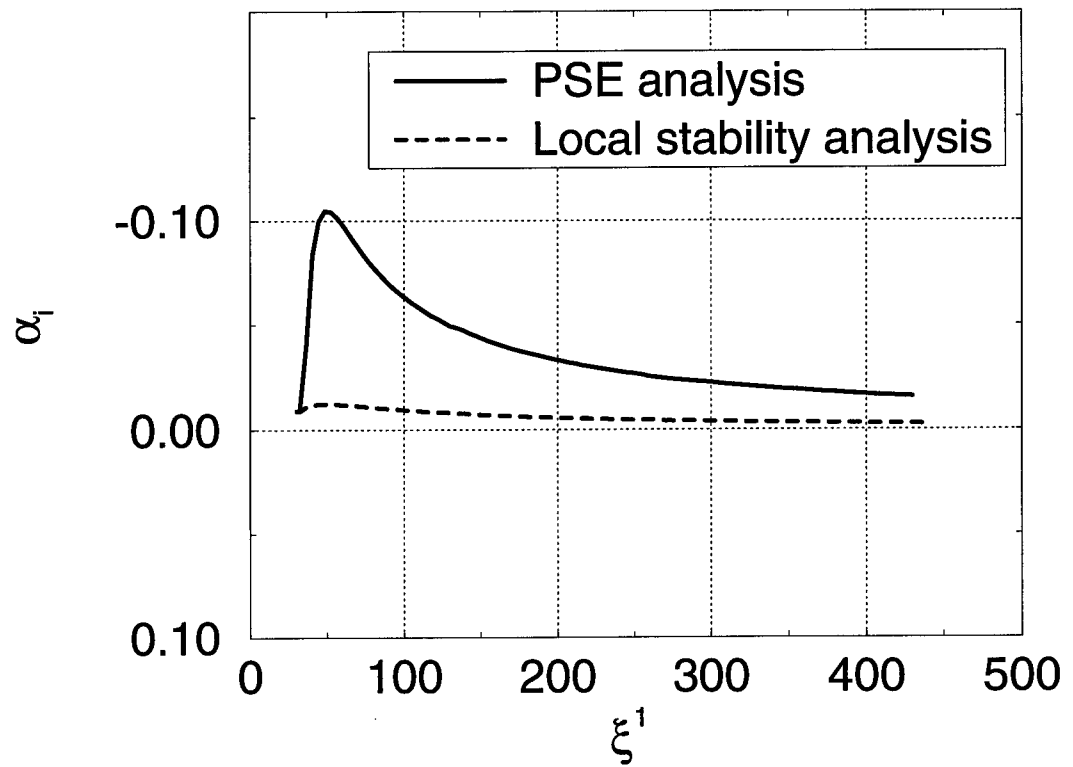


Figure 33: Growth rate of the stationary crossflow vortex at $\theta = 72^\circ$ and $\beta = 30$.

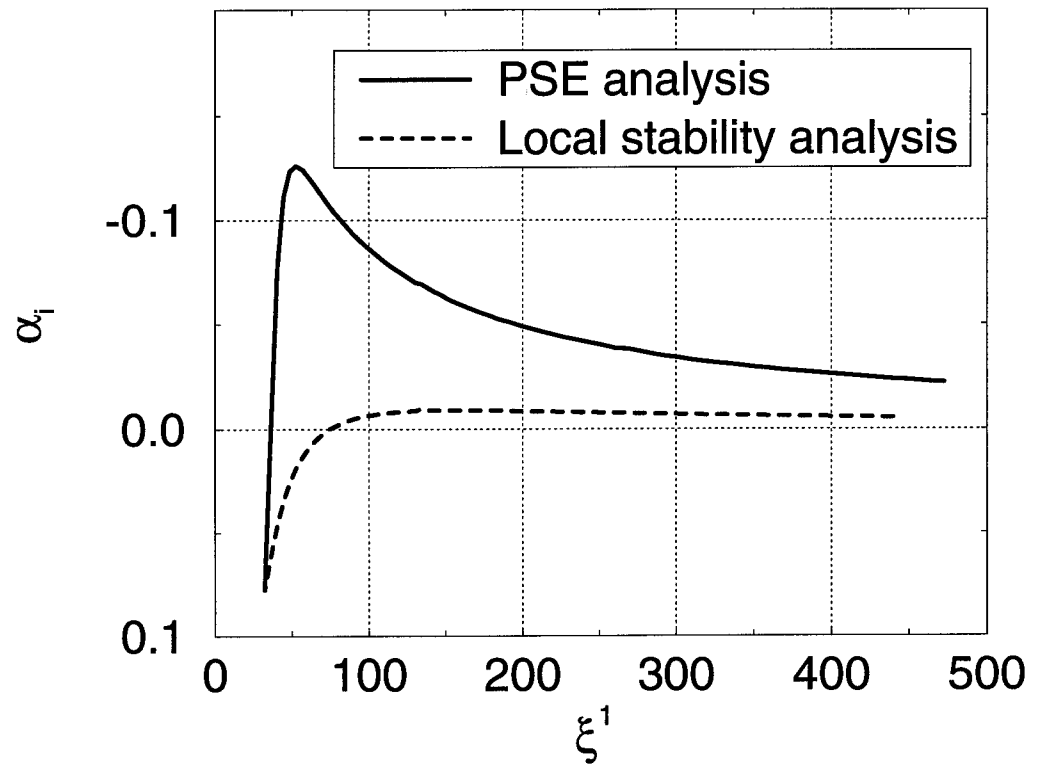


Figure 34: Growth rate of the stationary crossflow vortex at $\theta = 72^\circ$ and $\beta = 60$.

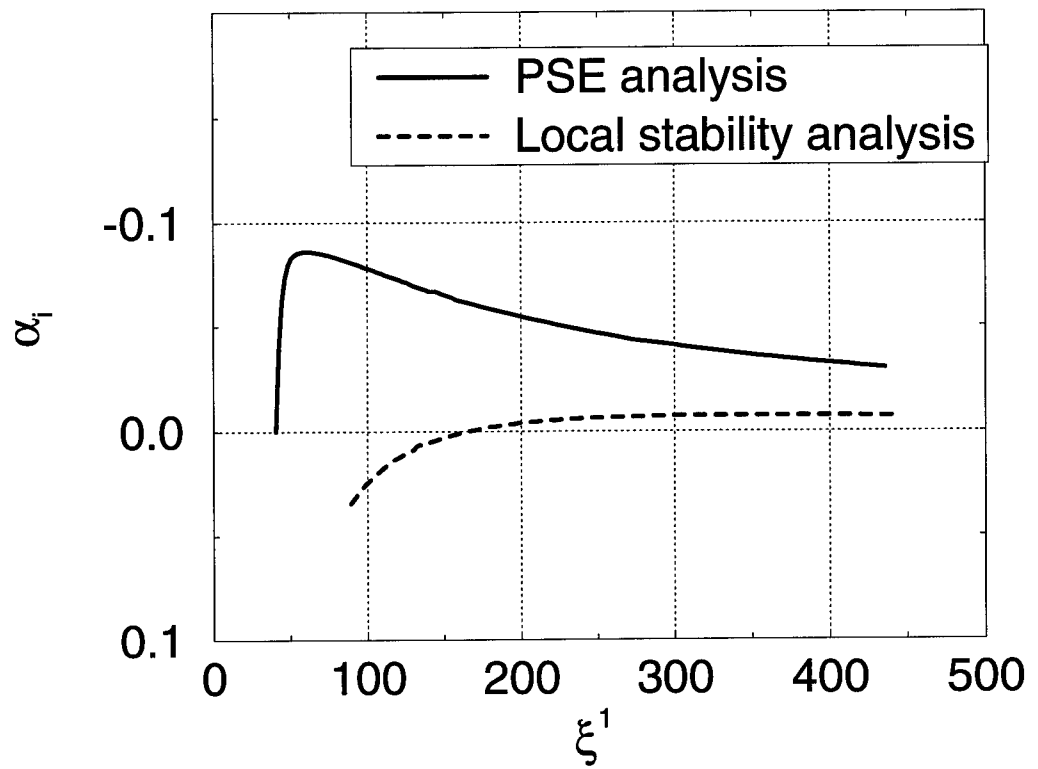


Figure 35: Growth rate of the stationary crossflow vortex at $\theta = 72^\circ$ and $\beta = 100$.

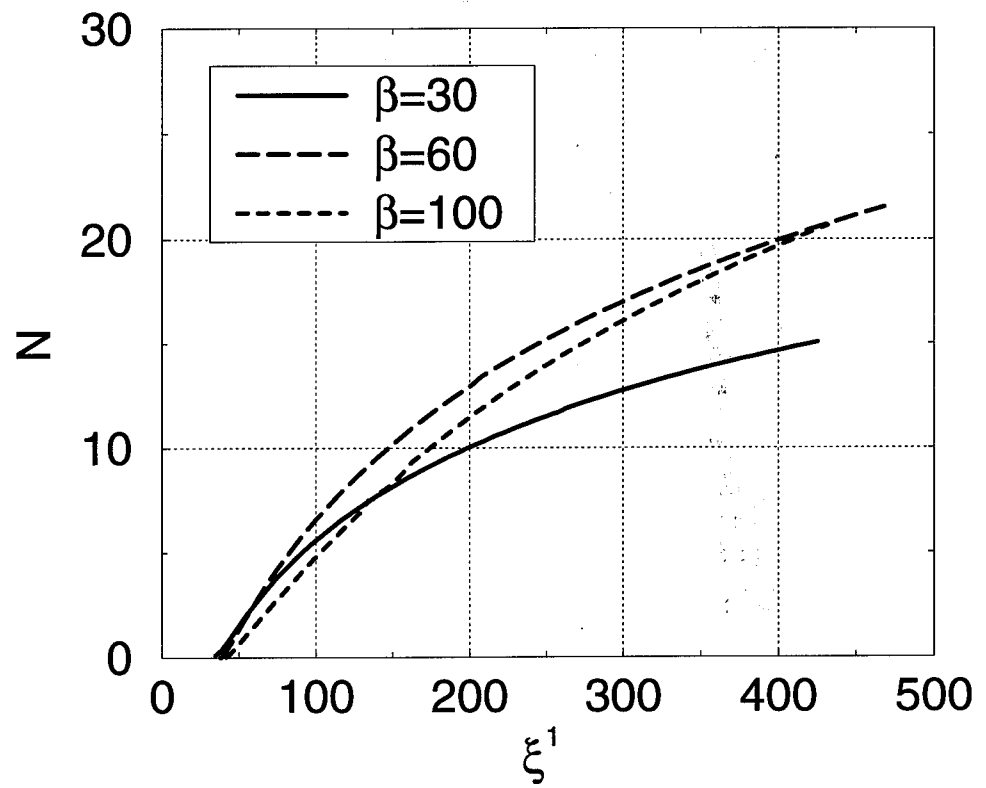


Figure 36: PSE result for the N factor of stationary crossflow vortices at $\theta = 72^\circ$.